## **Cutting Forces in Milling Processes**

#### 1.1. Formulations of cutting forces

Milling is a cutting operation which is generally used to remove materials from the blank for the purpose of achieving parts with the desired shape and surface quality. Cutting mechanics of the milling process includes the shearing effect between the cutting edge and the workpiece, the friction effect between the rake face and chip, as well as the ploughing effect between the clearance surface and the machined surface. The combined influence of the three effects lead to the generation of cutting forces, which can result in cutting deflections and can further damage the surface quality of the machined parts. Study of the mechanics of the milling process is of great significance to control surface errors and to plan stable cutting strategy. Milling is a typical multipoint tool operation, whose cutting mechanism involves elastic-plastic mechanics and thermal dynamics. Specific analyses for a detailed understanding of the behavior of temperature and strain rate fields are not covered in this text. In this chapter, we will discuss the generation mechanism of cutting forces, and then detail a series of methods for calibrating the cutting force coefficients which enable us to accurately predict cutting forces.

## 1.1.1. Mechanics of orthogonal cutting

Orthogonal cutting is usually used to explain the mechanism of material removal, and the three-dimensional oblique cutting process can be evaluated by geometrical and kinematic transformation models, as reported by Altintas [ALT 12]. Without the loss of generality, the orthogonal cutting process is

adopted to formulate the cutting forces. Figure 1.1 shows the relationship of cutting forces in the cross-sectional view of an orthogonal cutting process. The cutting edge is assumed to be a sharp one so that the shearing effect occurs at a plane without thickness. Two cutting force components exist between the chip and tool (i.e. the normal  $F_n$  and the friction  $F_f$  components). They are in balance with the normal and shearing force components related to the shear plane, i.e.  $F_{nshear}$  and  $F_{shear}$ , as shown in Figure 1.1(a).

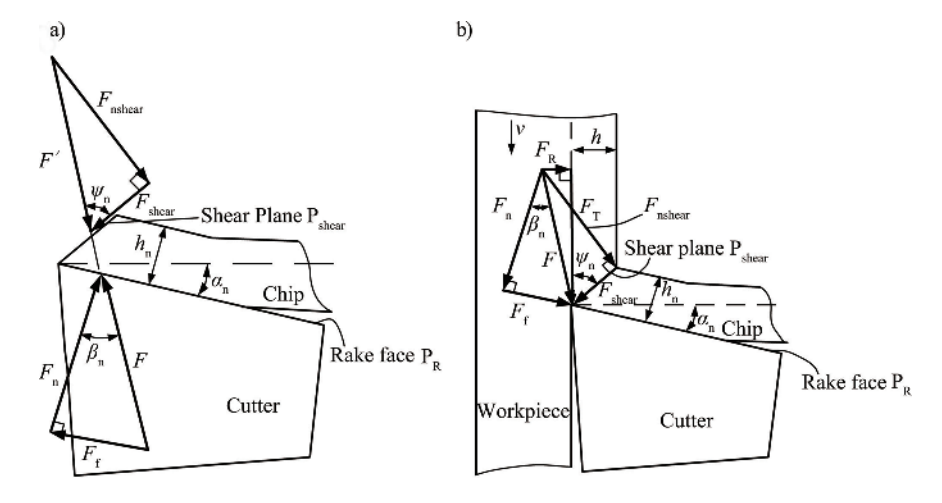


Figure 1.1. Cutting forces in the orthogonal cutting process

Shearing force  $F_{\text{shear}}$  can be expressed as

$$F_{\text{shear}} = \tau_{\text{s}} bh / \sin \psi_{\text{n}} \tag{1.1}$$

where h is the instantaneous uncut chip thickness and b is the chip width.  $\tau_s$  is the yield shearing stress of the workpiece material.  $\psi_n$  is the shearing angle defined as the angle between the shear plane and the cutting speed.

From Figure 1.1, it can be observed that

$$F_{\text{shear}} = F\cos(\psi_{\text{n}} + \beta_{\text{n}} - \alpha_{\text{n}})$$
 [1.2]

where F is the resultant cutting force and  $\beta_n$  is the friction angle, measured as the angle between F and  $F_n$ ,  $\alpha_n$  is the normal rake angle of the cutter.

Combination of equation [1.1] and equation [1.2] gives rise to

$$F = \frac{\tau_{s}bh}{\sin\psi_{n}\cos(\psi_{n} + \beta_{n} - \alpha_{n})}$$
 [1.3]

At the same time, F can be also split into tangential force  $F_{\rm T}$  parallel to the cutting speed direction, and component  $F_{\rm R}$  normal to the cutting speed direction.

$$F_{\rm T} = F \cos(\beta_{\rm n} - \alpha_{\rm n})$$

$$F_{\rm R} = F \sin(\beta_{\rm n} - \alpha_{\rm n})$$
[1.4]

The substitution of equation [1.3] into equation [1.4] produces

$$F_{\rm T} = K_{\rm T}bh$$

$$F_{\rm R} = K_{\rm R}bh$$
[1.5]

with

$$K_{\rm T} = \frac{\tau_{\rm s} \cos(\beta_{\rm n} - \alpha_{\rm n})}{\sin \psi_{\rm n} \cos(\psi_{\rm n} + \beta_{\rm n} - \alpha_{\rm n})}$$

$$K_{\rm R} = \frac{\tau_{\rm s} \sin(\beta_{\rm n} - \alpha_{\rm n})}{\sin \psi_{\rm n} \cos(\psi_{\rm n} + \beta_{\rm n} - \alpha_{\rm n})}$$
[1.6]

Equation [1.5] means that the cutting forces can be evaluated by multiplying bh, the cross area of the chip, by the cutting force coefficients  $K_{\rm T}$  or  $K_{\rm R}$  expressed by equation [1.6], derived from the shearing mechanism. In the actual cutting experience, the total cutting forces are contributed by the shearing effect related to the primary and secondary deformation zones, and the "ploughing" or "rubbing" effect at the flank of the cutting edge, which is associated with the tertiary deformation zone. Due to this fact, there are two widely used cutting force models depending upon whether the rubbing effect is included or not. The first one is the so-called lumped mechanism model

that shares the same mathematical equation as equation [1.5]. As its name suggests, the shearing on the rake face and the rubbing at the cutting edge are merged as a single coefficient. The second model is the dual mechanism model, which calculates the cutting forces as a superposition of shearing and edge forces with

$$F_{\rm T} = K_{\rm Tc}bh + K_{\rm Te}b$$

$$F_{\rm R} = K_{\rm Rc}bh + K_{\rm Re}b$$
[1.7]

where  $K_{Tc}$  or  $K_{Rc}$  represents the cutting coefficient due to shearing effect, while  $K_{\text{Te}}$  or  $K_{\text{Re}}$  stands for the edge coefficient that does not contribute to the shearing. The first term of the right-hand side of equation [1.7] is obtained by applying the same mechanism of orthogonal cutting mechanics as explained in equation [1.5].

It is noted that equation [1.6] is derived from the orthogonal cutting operation. In the oblique cutting process, cutting force coefficients are calculated by the orthogonal-to-oblique method. Readers are referred to the well-known formulas developed in [ALT 12] for the details of the orthogonal-to-oblique method.

If the materials property parameter  $\tau_s$ , cutter geometrical parameter  $\alpha_n$ , process geometrical parameters  $\psi_n$  and  $\beta_n$ , and the cutting condition parameters b and h are known in advance, the values of cutting force coefficients  $K_T$  and  $K_R$  (or  $K_{Tc}$  and  $K_{Rc}$ ) can be calculated by using the analytical equation [1.6]. Alternatively,  $K_T$  and  $K_R$  (or  $K_{Tc}$  and  $K_{Rc}$ , and  $K_{\text{Te}}$  and  $K_{\text{Re}}$ ) can also be mechanistically identified based on the measured cutting forces. The following contents will detail the modeling of cutting forces in the milling process and the related methods for obtaining the values of cutting force coefficients.

## 1.1.2. Cutting force model for a general milling cutter

A general end milling cutter with helical flutes is shown in Figure 1.2. XYZ is the coordinate system, with the positive direction of axes Y and X being aligned with the normal direction of the machined surface and the feed direction, respectively. D, R,  $R_r$ ,  $R_z$ ,  $\alpha_1$ ,  $\alpha_2$  and H are seven geometric parameters [ENG 01, GRA 04] used to describe the cutter envelope. Note that in Figure 1.2,  $M_{\rm z}$ ,  $N_{\rm z}$ ,  $M_{\rm r}$  and  $N_{\rm r}$  are geometrical parameters that can be calculated by these seven parameters. As explained in [ENG 01], distinct cutter geometries can be deduced from the general end mill model when particular values are attributed to these parameters. For example, parameters  $\{D, R, R_{\rm r}, R_{\rm z}, \alpha_1, \alpha_2, H\}$  will be chosen as  $\{D, 0, D/2, 0, 0, 0, H\}$  and  $\{D, D/2, 0, D/2, 0, 0, H\}$  for the flat end and ball end mills, respectively.

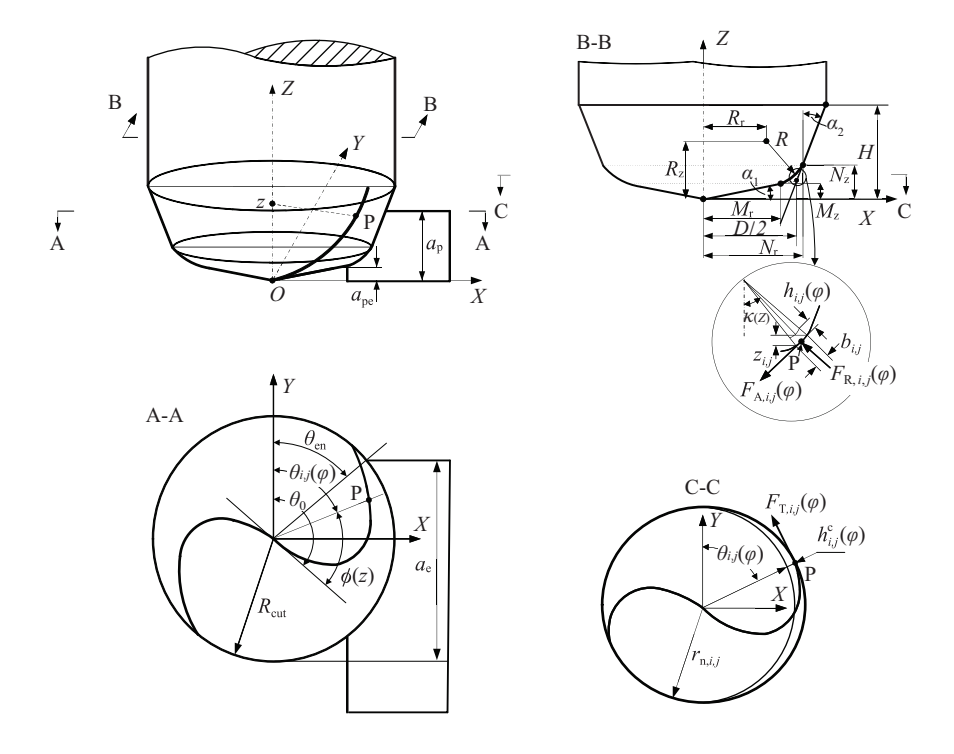


Figure 1.2. Geometric model of a general end mill and the cutting process

For the convenience of cutting force calculation, the cutting edges are divided into a finite number of co-axial disk elements with equivalent axial length. For convenience, the axial length of the jth axial disk element of the ith flute is symbolized as  $z_{i,j}$ . It should be noted that  $z_{i,j} = z_{i,k}$  (k=1, 2, ...). The total cutting forces are summed axially along the sliced disk elements from the bottom of the flute to the final axial depth of cut. The cutting forces

contributed by the *j*th axial disk element of the *i*th flute (e.g. the element P shown in Figure 1.2) at an arbitrary cutter rotation angle  $\varphi$  can be expressed by the lumped or dual mechanism models.

Lumped mechanism model

$$F_{\mathrm{T},i,j}(\varphi) = K_{\mathrm{T}} h_{i,j}(\varphi) b_{i,j}$$

$$F_{\mathrm{R},i,j}(\varphi) = K_{\mathrm{R}} h_{i,j}(\varphi) b_{i,j}$$

$$F_{\mathrm{A},i,j}(\varphi) = K_{\mathrm{A}} h_{i,j}(\varphi) b_{i,j}$$
[1.8]

with

$$h_{i,j}(\varphi) = h_{i,j}^{c}(\varphi) \sin \kappa(z)$$

$$b_{i,j} = z_{i,j} / \sin \kappa(z)$$
[1.9]

where  $K_{\rm T}$ ,  $K_{\rm R}$ ,  $K_{\rm A}$  are three cutting force coefficients in tangential, radial and axial directions.  $h_{i,j}(\varphi)$  and  $\kappa(z)$  are the instantaneous uncut chip thickness at the current cutter rotation angle  $\varphi$  and the tool cutting edge angle related to the jth axial disk element of the ith flute, respectively. z is the axial coordinate of the jth axial disk element of the ith flute. Based on the geometric definition of the general end mill,  $\kappa(z)$  can be expressed as follows [GRA 04].

Case 1: if  $z \leq M_z$ ,

$$\kappa(z) = \alpha_1$$

$$\phi(z) = \ln[z/\tan \alpha_1] \tan \beta/\cos \alpha_1$$
[1.10]

where  $\phi(z)$  is the radial lag angle at z due to the cutter helix angle  $\beta$ .

Case 2: if  $M_z < z \le N_z$ ,

$$\kappa(z) = \arcsin \sqrt{1 - [(R_z - z)/R]^2}$$

$$\phi(z) = (z - M_z) \tan \beta / R + \ln(M_r) \tan \beta / \cos \alpha_1$$
[1.11]

Case 3: if  $N_z < z$ ,

$$\kappa(z) = \pi/2 - \alpha_2$$

if 
$$\alpha_2 \neq 0$$

$$\phi(z) = \phi_0 + \ln[(N_r + z - N_z) \tan \alpha_2] \tan \beta / \sin \alpha_2 - \ln(N_r) \tan \beta / \sin \alpha_2$$

if  $\alpha_2 = 0$ 

$$\phi(z) = \phi_0 + (z - N_z) \tan \beta / N_r$$

$$\phi_0 = (N_z - M_z) \tan \beta / R + \ln(M_r) \tan \beta / \cos \alpha_1$$
[1.12]

Dual mechanism model

$$F_{\mathrm{T},i,j}(\varphi) = K_{\mathrm{Tc}} h_{i,j}(\varphi) b_{i,j} + K_{\mathrm{Te}} b_{i,j}$$

$$F_{\mathrm{R},i,j}(\varphi) = K_{\mathrm{Rc}} h_{i,j}(\varphi) b_{i,j} + K_{\mathrm{Re}} b_{i,j}$$

$$F_{\mathrm{A},i,j}(\varphi) = K_{\mathrm{Ac}} h_{i,j}(\varphi) b_{i,j} + K_{\mathrm{Ae}} b_{i,j}$$
[1.13]

where  $K_{qc}$  and  $K_{qe}$  (q=T, R or A) are the force coefficients corresponding to the chip shearing and the edge rubbing, respectively.

Once three force components are obtained from equation [1.8] or equation [1.13], they can be mapped along the X, Y and Z directions as

$$\begin{bmatrix}
F_{X,i,j}(\varphi) \\
F_{Y,i,j}(\varphi) \\
F_{Z,i,j}(\varphi)
\end{bmatrix} = g(\theta_{i,j}(\varphi))\mathbf{T}(\theta_{i,j}(\varphi)) \begin{bmatrix}
F_{T,i,j}(\varphi) \\
F_{R,i,j}(\varphi) \\
F_{A,i,j}(\varphi)
\end{bmatrix}$$
[1.14]

with

$$\mathbf{T}(\theta_{i,j}(\varphi)) = \begin{bmatrix} -\cos\theta_{i,j}(\varphi) & -\sin\kappa(z)\sin\theta_{i,j}(\varphi) & -\cos\kappa(z)\sin\theta_{i,j}(\varphi) \\ \sin\theta_{i,j}(\varphi) & -\sin\kappa(z)\cos\theta_{i,j}(\varphi) & -\cos\kappa(z)\cos\theta_{i,j}(\varphi) \\ 0 & \cos\kappa(z) & -\sin\kappa(z) \end{bmatrix}$$

where  $\theta_{i,j}(\varphi)$  is the cutter position angle related to the *j*th axial disk element of the *i*th flute at cutter rotation angle  $\varphi$ , and is defined as the clockwise angle determined from axis Y to the disk element.  $g(\theta_{i,j}(\varphi))$  is the window function used to identify whether the disk element is in cut or not.

$$g(\theta_{i,j}(\varphi)) = \begin{cases} 1, & \theta_{\mathrm{en},i,j}(\varphi) \le \theta_{i,j}(\varphi) \le \theta_{\mathrm{ex},i,j}(\varphi) \\ 0, & \text{otherwise} \end{cases}$$
 [1.15]

where  $\theta_{\text{en},i,j}(\varphi)$  and  $\theta_{\text{ex},i,j}(\varphi)$  are entry and exit angles related to the *j*th axial disk element of the *i*th flute, which are geometrically defined in Figure 1.3

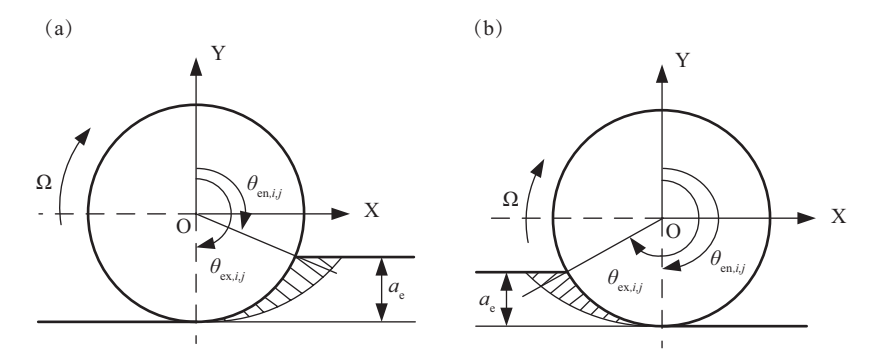


**Figure 1.3.** Definition of entry and exit angles: a) down milling; b) up milling

Subsequently, the total cutting force components  $F_s(\varphi)$  (s=X, Y or Z) at any cutter rotation angle  $\varphi$  can be evaluated by summing the forces acting on all flutes and disk elements:

$$F_s(\varphi) = \sum_{i,j} F_{s,i,j}(\varphi) , \quad s = X, Y \text{ or } Z$$
 [1.16]

## 1.2. Milling process geometry

## 1.2.1. Calculations of uncut chip thickness

As illustrated in Figure 1.4, at an instantaneous cutting position of the jth axial disk element of the ith flute, the equivalent chip thickness  $h_{i,j}^c(\varphi)$  refers to the distance in the radial direction of the cutter between the tooth path to be generated by the cutter element, and the surface left by the jth axial disk element of the (i-m)th flute. The occurrence of cutter runout will lead to  $m \neq 1$ . Due to the deflections of the cutter and workpiece, the cutter axis shifts from its nominal position. As a result, two adjacent tooth paths will deviate from the desired paths. So,  $h_{i,j}^c(\varphi)$  will be different from the nominal value. Based on

the circular tooth path assumption [MAR 45] shown in Figure 1.4(a),  $h_{i,j}^{\rm c}(\varphi)$  is calculated as follows

$$h_{i,j}^{c}(\varphi) = r_{i,j} - l_{i,j}$$
 [1.17]

where  $l_{i,j}$  is an intermediate variable, as shown in Figure 1.4.  $r_{i,j}$  is the actual radius of the circular tooth path generated by the jth axial disk element of the ith flute at cutter rotation angle  $\varphi$ . In this section,  $r_{i,j}$  will be calculated by using equation [1.18] based on the radial cutter runout model, which is widely used by many researchers [WAN 03, ARM 89, LIA 94, FEN 94a, FEN 94b, WAN 07a, AKS 98, AZE 04, CHE 97, SEE 99, SHI 97, WAN 07b, WAN 94].

$$r_{i,j} = r_{\text{n},i,j} + \rho \cos[\lambda - \phi(z) - 2(i-1)\pi/N]$$
 [1.18]

where  $r_{\mathrm{n},i,j}$  is the nominal cutting radius of the *j*th axial disk element of the *i*th flute. N is the total number of cutting teeth of the cutter.  $\rho$  and  $\lambda$  are the geometrical parameters in the radial cutter runout model, in which the cutter axis is assumed to be parallel to the centerline of the machine spindle, as defined in Figure 1.5. Geometrically,  $\rho$  is the cutter axis offset, defined as the distance between the rotation center of the spindle and the geometric center of the cutter, while  $\lambda$  is location angle measured as the angle between the direction of the offset and the tip of the nearest tooth (tooth 1).

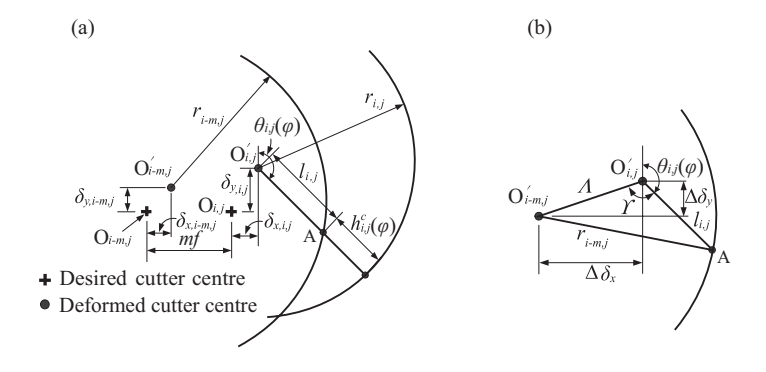


**Figure 1.4.** Geometric illustration of equivalent chip thickness: a) geometric definition; b) close-up view of sub-figure (a)

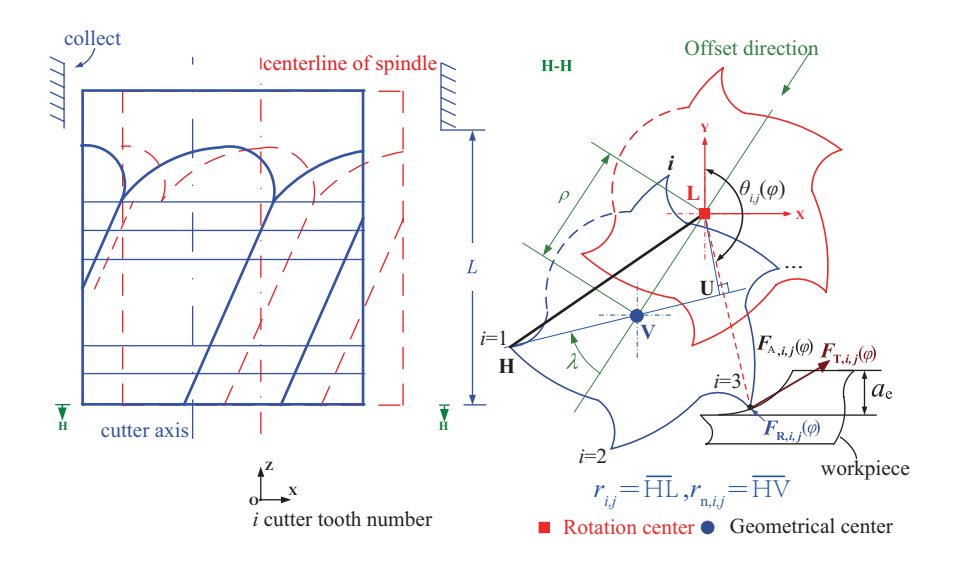


Figure 1.5. Definition of radial cutter runout. For a color version of this figure, see www.iste.co.uk/zhang/milling.zip

Using the law of cosines, a geometric relation exists between the cutter centre of the current tooth path and that of the past tooth path in Figure 1.4(b).

$$r_{i-m,j}^2 = \Lambda^2 + l_{i,j}^2 - 2\Lambda l_{i,j} \cos \Upsilon$$
 [1.19]

in which

$$\Lambda = \sqrt{\Delta \delta_x^2 + \Delta \delta_y^2}$$
 [1.20]

with

$$\Delta \delta_x = mf + \delta_{x,i,j} - \delta_{x,i-m,j}; \ \Delta \delta_y = \delta_{y,i,j} - \delta_{y,i-m,j}$$
 [1.21]

Notice that  $(\delta_{x,i,j}, \delta_{y,i,j})$  and  $(\delta_{x,i-m,j}, \delta_{y,i-m,j})$  correspond to offset values of cutter centres of the current tooth and the m-past tooth from their

desired positions, respectively. f is the feed per tooth. Obviously, the following relation holds.

$$\Upsilon = \pi - \theta_{i,j}(\varphi) + \arccos(\frac{\Delta \delta_y}{\Lambda})$$
 [1.22]

By solving equation [1.19],  $l_{i,j}$  is obtained as

$$l_{i,j} = \Lambda \cos \Upsilon + \sqrt{r_{i-m,j}^2 - \Lambda^2 \sin^2 \Upsilon}$$
 [1.23]

By substituting equation [1.23] into equation [1.17],  $h_{i,j}^{c}$  is derived as

$$h_{i,j}^{c}(\varphi) = -\Lambda \cos \Upsilon + r_{i,j} - \sqrt{r_{i-m,j}^{2} - \Lambda^{2} \sin^{2} \Upsilon}$$
 [1.24]

Due to the fact that  $r_{i-m,j} >> \Delta \delta_x$  and  $r_{i-m,j} >> \Delta \delta_y$ , it follows that  $r_{i-m,j} >> \Lambda \sin \Upsilon$  from equation [1.20]. Thus, equation [1.24] can be approximated by

$$h_{i,j}^{c}(\varphi) = -\Lambda \cos \Upsilon + r_{i,j} - r_{i-m,j}$$

$$\approx mf \sin \theta_{i,j}(\varphi) + r_{i,j} - r_{i-m,j}$$
[1.25]

Note that if a negative value of  $h_{i,j}^{\rm c}(\varphi)$  is obtained by equation [1.24] or equation [1.25],  $h_{i,j}^{\rm c}(\varphi)$  is set to be zero.

Physically, a static milling process free of vibration implies that cutting forces must have stabilized themselves after a few tooth periods. In other words, the cutting forces obtained from two adjacent tooth periods must be equal, as assumed by Budak [BUD 92]. The implication of this stability condition requires that the volume of materials cut off by the current tooth should be identical to that cut off by the previous tooth with the negligence of runout, i.e. m=1 and  $r_{i,j}=r_{i-1,j}$  in equation [1.25]. Now, suppose that  $F_i(\theta_{i,j}(\varphi))$  represents the resultant cutting force vector associated with the cutter position angle  $\theta_{i,j}(\varphi)$ , then

$$\mathbf{F}_{i}(\theta_{i,j}(\varphi)) = \mathbf{F}_{i-1}(\theta_{i-1,j}(\varphi))$$
[1.26]

Likewise, cutter deflections of the concerned cutter segment also remain unchanged between two adjacent teeth, so that following equations hold

$$\delta_{t,i,j} = \delta_{t,i-1,j} \tag{1.27}$$

where  $\delta_{t,i,j} = (\delta_{t,X,i,j}, \delta_{t,Y,i,j}, \delta_{t,Z,i,j})$  is the cutter deflection vector corresponding to the *j*th axial disk element of the *i*th flute. It is evaluated based on the cantilevered beam model [SUT 86, BUD 95, SHI 96].

Concerning the cutter center offset values  $(\delta_{x,i,j}, \delta_{y,i,j}, \delta_{x,i-1,j}, \delta_{y,i-1,j})$ , because of  $\delta_{x,i,j} = \delta_{t,X,i,j}$  and  $\delta_{y,i,j} = \delta_{t,Y,i,j}$ , the following important relations can be derived:

- from equation [1.27],

$$\delta_{x,i,j} = \delta_{x,i-1,j}, \ \delta_{y,i,j} = \delta_{y,i-1,j}$$
 [1.28]

- from equation [1.21],

$$\Delta \delta_x = f, \ \Delta \delta_y = 0 \tag{1.29}$$

- from equation [1.22],

$$\beta = \frac{3\pi}{2} - \theta_{i,j}(\varphi) \tag{1.30}$$

By reviewing the above relations, equation [1.25] can be further simplified as

$$h_{i,j}^{c}(\varphi) = f \sin \theta_{i,j}(\varphi)$$
 [1.31]

Obviously, equation [1.31] indicates that  $h_{i,j}^c$  converges to its nominal value of  $f\sin\theta_{i,j}(\varphi)$  in a static milling process. It gives the theoretical explanation why the nominal value of the equivalent chip thickness,  $f\sin\theta_{i,j}(\varphi)$ , is widely used by many researchers to establish the cutting force model.

## 1.2.2. Determination of entry and exit angles

Equation [1.15] shows that cutting force prediction is dependent on the entry,  $\theta_{en}$ , and the exit,  $\theta_{ex}$ , angles. In the case of a milling workpiece with

simple geometry, both angles can be calculated analytically. For instance, in flat end milling of a plane, the entry and exit angles can be mathematically expressed as

$$\theta_{\rm en} = \frac{\pi}{2} + \arcsin \frac{(D - 2a_{\rm e})}{D}, \ \theta_{\rm ex} = \pi,$$
 for down milling 
$$\theta_{\rm en} = \pi, \ \theta_{\rm ex} = \frac{\pi}{2} - \arcsin \frac{(D - 2a_{\rm e})}{D},$$
 for up milling [1.32]

where  $a_e$  stands for the radial depth of cut.

For a milling workpiece with complex geometry, a complicated cutter geometry and process geometry make it very difficult to analytically determine the entry and exit angles. Alternatively, researchers propose that through extracting the cutter-workpiece engagement (CWE) region, i.e. the engagement domain of each axial disk along the tool axis, the entry and exit angles can be correspondingly calculated. A literature review shows that existing CWE extracting methods have the following characteristics:

- for a discrete method [CHO 97, LAZ 03, FUS 03, ROT 07, LI 10, ZHA 11, ARA 11, KIM 06, LI 08, KAR 10], the achievement of high accuracy computing of CWE requires a high resolution of workpiece decomposition, large store memory and long computing time;
- for a solid modeling-based method [FER 08b, LAZ 11, SPE 94, IMA 98, ELM 98, SPE 00, YIP 06], Boolean operations for implementing surface/surface intersection algorithms are greatly time-consuming because CWE maps are extracted from the in-process workpiece. Meanwhile, as the data structure size quickly increases during simulation, numerical inaccuracies of the workpiece's model will be stacked and thus topological errors may occur.

This section proposes a solid trimming method by which CWE maps are extracted from the removal volume of multi-axis milling rather than from the in-process workpiece (IPW). In this method, both the workpiece and tool surfaces are described by a B-rep solid modeler.

CWE is geometrically defined as the instantaneous engagement region when flutes enter into and leave a workpiece. In other words, it is the contact area between the tool envelope surface and the workpiece, and can be treated as a function of cutter's axial height. The calculation of CWE thus depends upon both the geometry complexities of the cutter and workpiece as well as the relative location between the cutter and workpiece. It is independent of tool flute numbers and cutting parameters. The proposed method is schematically depicted in Figure 1.6. It can be seen that the calculation of CWE maps is based on the removal volume, rather than the entire in-process workpiece, as reported in [ARA 08]. This allows the subsequent operations to be performed on a simple data structure. Detailed explanations of the key steps are described below.

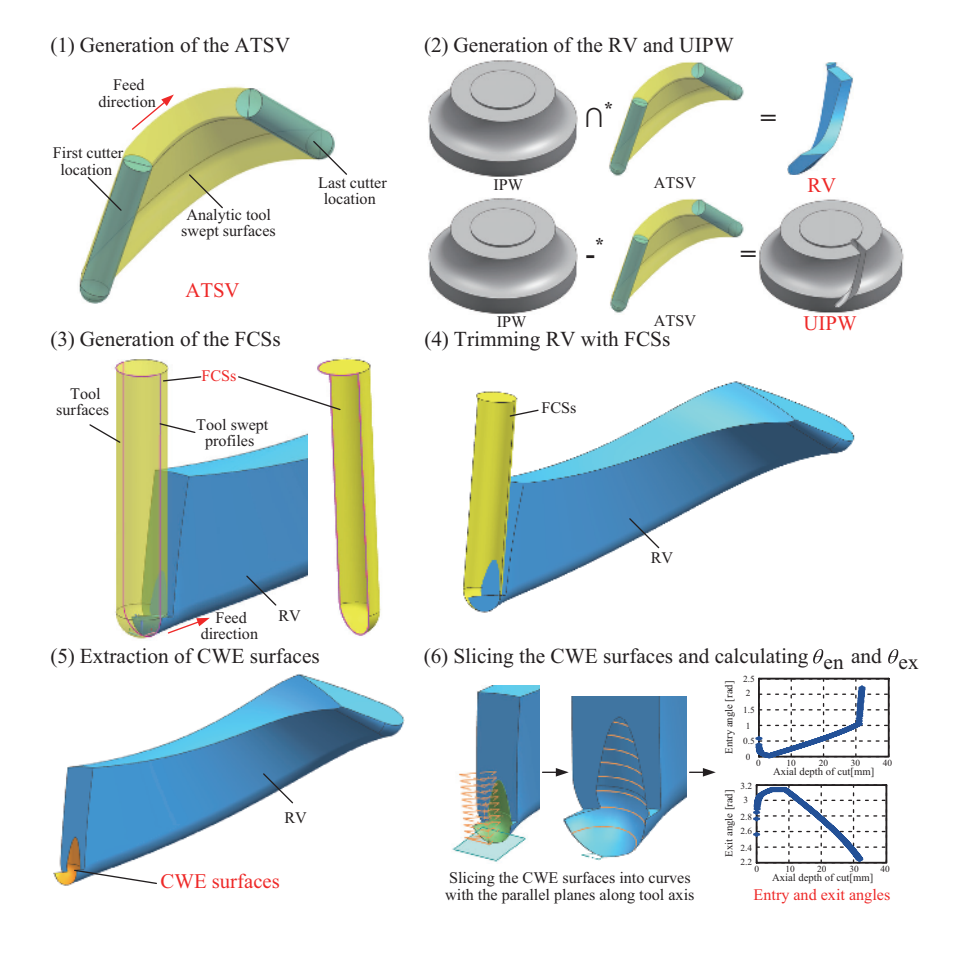


Figure 1.6. The whole procedure of CWE extraction. For a color version of this figure, see www.iste.co.uk/zhang/milling.zip

# 1.2.2.1. Generation of analytic tool swept volume, removal volume and updated in-process workpiece

This section corresponds to steps (1) and (2) in Figure 1.6. The main content of both steps are as follows:

i) Generation of the analytic tool swept volume (ATSV) by the method reported in [WEI 04]. This step is often performed by sewing the analytic tool swept surface,  $\{\text{Faces}\}_{\text{Swept}}$ , the ingress part of the tool surface,  $\{\text{Faces}\}_{\text{Egress}}$ , at the first cutter location and the egress part of the tool surface,  $\{\text{Faces}\}_{\text{Egress}}$ , at the  $(N_{CL}-1)$ th cutter location,

$$E_{\text{Swept}} = \{\text{Faces}\}_{\text{Swept}} + \{\text{Faces}\}_{\text{Ingress}} + \{\text{Faces}\}_{\text{Egress}}$$
 [1.33]

where  $E_{\rm Swept}$  denotes the solid model of analytic tool swept volume.  $N_{CL}$  denotes the number of cutter locations.

In this work, the analytic tool swept surface is obtained by employing the analytic method proposed in [GON 09].

ii) With the ATSV obtained above, the removal volume (RV) and updated in-process workpiece (UIPW) are obtained by performing Boolean operations between the ATSV and the in-process workpiece (IPW):

$$RV = ATSV \bigcap^* IPW$$
 [1.34]

$$UIPW = IPW - *ATSV$$
 [1.35]

where  $\bigcap^*$  and  $-^*$  denote the Boolean intersection and subtraction operator, respectively. Notice that UIPW becomes IPW for the next tool path segments.

Traditionally, equation [1.34] is carried out based on the tool swept volume obtained with Boolean union operation among the cutter solid models at all cutter locations along the tool path [FER 08a]. Because there are many small edges and faces in the tool swept volume, the calculation of RV needs many surface/surface intersection calculations between the IPW and the tool swept volume, whereas the method proposed here determines RV by using the ATSV, which involves at most nine surfaces. As a result, abundant surface/surface intersection calculations are avoided in the calculation procedure of RV and UIPW. Correspondingly, the simple data structure of the ATSV results in a

simple data structure of the RV and UIPW. This favors the efficient CWE extraction described in the following sections.

#### 1.2.2.2. Generation of the feasible contact surfaces

In the actual milling process, only partial tool surfaces may make contact with the workpiece, as illustrated in Figure 1.7(a). These surfaces are named feasible contact surfaces (FCSs) according to [ARA 08]. Mathematically, the angle between the tool surface normal  $\mathbf{N}(u,v,t)$  and the instantaneous velocity  $\mathbf{V}(u,v,t)$  at any point on FCSs of a tool should be a sharp or a right angle at most. That is,

$$\mathbf{N}(u, v, t) \cdot \mathbf{V}(u, v, t) \ge 0 \tag{1.36}$$

where u and v are two variables in the parameter equations of the tool surfaces. t is the instantaneous cutting time variable corresponding to the given cutter location. If a set of points meet the condition  $\mathbf{N}(u,v,t)\cdot\mathbf{V}(u,v,t)=0$ , these points will constitute closed curves, named tool swept profiles, which define the critical boundaries of FCSs, as shown in Figure 1.7(b). Then, the FCSs are obtained by following the two steps below. First, split the tool surfaces into two parts by the tool swept profiles. Second, select the part satisfying equation [1.36] as the required feasible contact surfaces  $\{\text{Faces}\}_{\text{FCS},k}$ , where k means the kth cutter location along the tool path.

## 1.2.2.3. Trimming removal volume with feasible contact surfaces

CWE surfaces are usually extracted by subtracting the tool movements from the solid model of the workpiece or the removal volume [LAZ 11]. As illustrated in Figure 1.8, some materials which should be removed from the workpiece are not actually cut, due to the inaccurate calculations of tool movements in 5-axis milling. This results in bodies with many small edges and surfaces being produced at each cutter location. As the cutter advances, these edges and faces will be accumulated along the tool path so that the model data structure and computing time will increase during the whole simulation procedure. Meanwhile, topological errors easily occur because of the stacked numerical inaccuracies induced by these small edges and faces.

Here the proposed method is to extract the CWE surfaces directly based on the removal volume and feasible contact surfaces obtained above. As shown in

- Figure 1.9, the trimming operation related to the kth cutter location is described below:
- 1) compute the intersection curves between the FCSs and boundary surfaces of RV;
- 2) split FCSs and the boundary surfaces of RV by the intersection curves obtained above;
- 3) reconstruct the remaining removal volume with the split boundary surfaces obtained above.

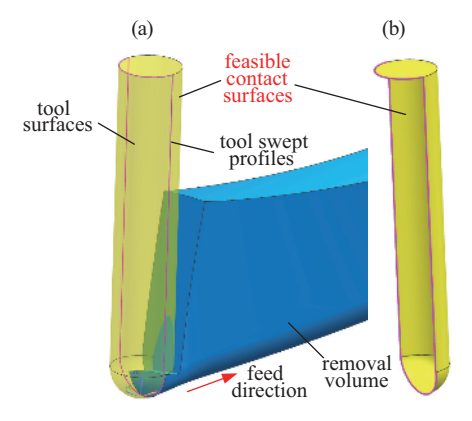
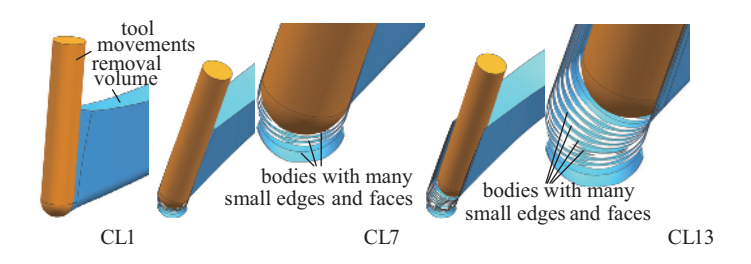


Figure 1.7. Illustration of feasible contact surfaces: a) tool surfaces contacting with the RV; b) feasible contact surfaces at specific cutter location. For a color version of this figure, see www.iste.co.uk/zhang/milling.zip



**Figure 1.8.** Production of bodies with many small edges and surfaces when the tool movements are subtracted from the removal volume. For a color version of this figure, see www.iste.co.uk/zhang/milling.zip

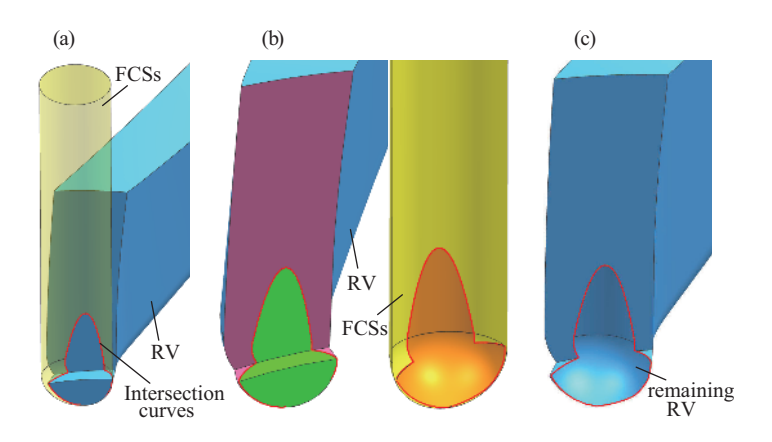


Figure 1.9. The illustration of the trimming operation: a) computing the intersection curves; b) splitting the boundary surfaces; c) reconstructing the remaining RV. For a color version of this figure, see www.iste.co.uk/zhang/milling.zip

In this way, a large number of bodies with small edges and faces can be avoided as the cutter moves along the tool path. Because only the FCSs of the tool surfaces may make contact with the workpiece in the actual milling process, the CWE surfaces are actually the subsets of the FCSs. Keeping this idea in mind, the CWE surfaces can be obtained through trimming the removal volume by the FCSs at each cutter location. With this operation, the CWE surfaces are directly imprinted on the remaining removal volume once the materials between the previous and the current FCSs are discarded. Following this procedure, CWE surfaces at the kth cutter location,  $\{Faces\}_{CWE,k}$ , can thus be expressed as

$$\{Faces\}_{CWE,k} = \{Faces\}_{RV,k} \cap^* \{Faces\}_{FCS,k}$$
 [1.37]

where  $\{Faces\}_{RV,k}$  denotes all boundary surfaces of the remaining removal volume  $RV_{k+1}$  at the kth cutter location, and  $RV_{k+1}$  denotes the solid model of the remaining removal volume after the trimming operation at the kth cutter location. Figure 1.10 illustrates the CWE surfaces extraction procedure associated with two adjacent cutter locations.

In fact, in B-rep solid modeler, the CWE surfaces constitute partial boundary surfaces of the remaining removal volume. Once the cutter moves to a new cutter location, CWE surfaces on the removal volume related to the previous cutter location are removed, and newly generated CWE surfaces will be updated as the boundary surfaces of the remaining removal volume, as shown in Figure 1.10(b) and (d). This can avoid generating abundant small edges and faces. In addition, the number of boundary surfaces of the removal volume does not always increase. Benefiting from this steady data structure, the proposed method is efficient without stacked numerical inaccuracies and topological errors.

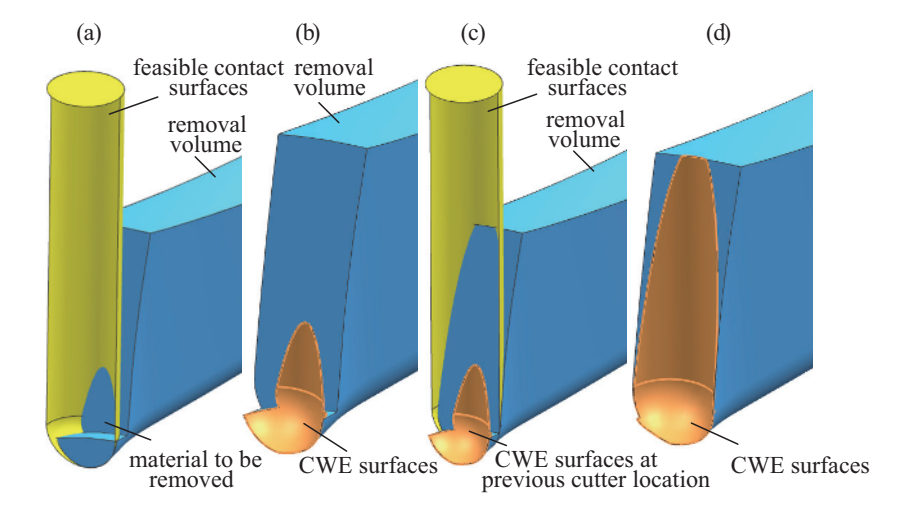


Figure 1.10. Illustration of trimming procedure: a) and c); instantaneous trimming status at the 1st and 2nd cutter locations; b) and d); remaining removal volume after trimming at the 1st and 2nd cutter locations. For a color version of this figure, see <a href="https://www.iste.co.uk/zhang/milling.zip">www.iste.co.uk/zhang/milling.zip</a>

#### 1.2.2.4. Extraction of the CWE surfaces from the removal volume

As described above, because CWE surfaces imprinted on some boundary surfaces of the remaining RV are generated by the FCSs, they have the same attributes as the tool surfaces, such as surface type, center point and axis direction. This means that these attributes can be used to identify and extract the CWE surfaces from the remaining RV. The detailed algorithm is described as follows.

- Step 1: search all boundary surfaces of the remaining removal volume  $RV_{k+1}$  at the kth cutter location and save them as  $\{Faces\}_{RV,k}$ .
  - Step 2: identify the surface attributes of all  $\{Faces\}_{RV,k}$ .
- Step 3: if the attributes of each  $\{Faces\}_{RV,k}$  are consistent with those of the tool surface, append the surface into the sequence of the CWE surfaces  $\{Faces\}_{CWE,k}$  at the kth cutter location.

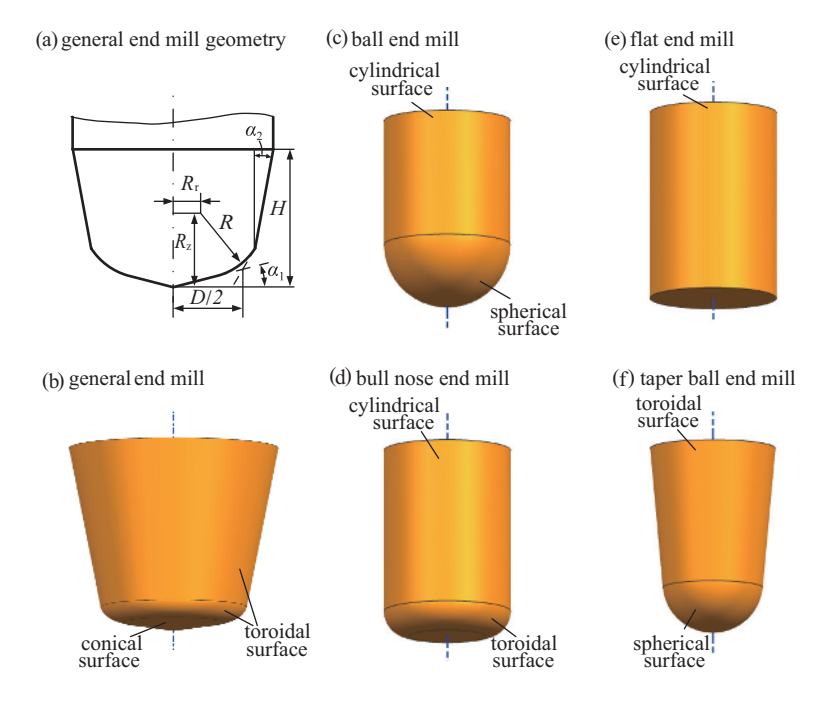


Figure 1.11. General tool geometry and surfaces of different end mills

For the different end mills shown in Figure 1.11, the types of tool surfaces can be classified as cylindrical, conical, toroidal and spherical surfaces, which include the attributes of axis, spherical center or radius, as listed in Table 1.1. With this information, one can perform Step 3 to identify the CWE surfaces. To have a clear understanding of the above method, the pseudo-codes corresponding to these milling cutters are described below.

#### **Input:**

 $RV_{k+1}$ : the remaining removal volume after trimming operation at the kth cutter location, where  $k=1,2,...,N_{CL}-1$ .

 $[\mathbf{P}_{c,k}, \mathbf{n}_k]$ : the cutter location data at the kth cutter location;  $\mathbf{P}_{c,k}$  denotes the cutter tip coordinate;  $\mathbf{n}_k$  denotes the tool orientation vector.

 $\epsilon$ : tolerance for comparing the constructive features of the surface and the cutter location.

 $\{D, R, R_r, R_z, \alpha_1, \alpha_2, H\}$ : tool geometry parameters as shown in Figure 1.11(a).

#### **Output:**

 $\{Faces\}_{CWE,k}$ : the CWE surfaces at the kth cutter location.

#### Step 1:

Search all boundary surfaces of the remaining removal volume  $RV_{k+1}$  at the kth cutter location and save them as  $\{Faces\}_{RV,k}$  temporarily.

#### Step 2:

FOR (each surface in  $\{Faces\}_{RV,k}$ )

{Identify the type of the surface, the axis of the revolution surface of the cutter body  $\mathbf{n}_s$ , and the sphere center of the revolution surface of the cutter body  $\mathbf{C}_s$ .}

#### Step 3:

IF

```
FOR (each surface in \{Faces\}_{RV,k}) 
{ IF (face type == cylindrical surface or face type == conical surface or face type == toroidal surface) 
{
```

$$\|\mathbf{n}_{s} - \mathbf{n}_{k}\|_{\infty} < \epsilon \text{ or } \|\mathbf{n}_{s} + \mathbf{n}_{k}\|_{\infty} < \epsilon$$
 [1.38]

{ Append the surface into the sequence of the cutter-workpiece engagement surfaces  $\{{\rm Faces}\}_{{\rm CWE},k}$  }

```
ELSE IF (face type == spherical surface)
```

Calculate the ball center  $C_{B,k}$  of the ball end mill or taper ball end mill with the cutter location data and tool geometry parameters, where

$$\mathbf{C}_{\mathrm{B},k} = \mathbf{P}_{\mathrm{c},k} - R\mathbf{n}_k \tag{1.39}$$

IF

$$(\|\mathbf{C}_{s} - \mathbf{C}_{B,k}\|_{\infty} < \epsilon) \tag{1.40}$$

```
{ Append the surface into the sequence of the cutter-workpiece engagement surfaces \{Faces\}_{CWE,k} } }.
```

Mill type	Surface type	Surface attributes
general end mill	toroidal surface	$axis(\mathbf{n}_k)$
	conical surface	$axis(\mathbf{n}_k)$
ball end mill	cylindrical surface	$axis(\mathbf{n}_k)$
	spherical surface	spherical center ( $\mathbf{C}_{\mathrm{B},k}$ )
bull nose end mill	cylindrical surface	$axis(\mathbf{n}_k)$
	toroidal surface	axis $(\mathbf{n}_k)$
flat end mill	cylindrical surface	$axis(\mathbf{n}_k)$
taper ball end mill	toroidal surface	$axis(\mathbf{n}_k)$
	spherical surface	spherical center ( $C_{B,k}$ )

Table 1.1. Surface attributes for different end mills

#### 1.2.2.5. Procedure for calculating entry and exit angles

The whole procedure for calculating the entry and exit angles for a specified workpiece model and cutter location (CL) file is summarized as follows:

- 1) read the information about cutter location, cutter geometry parameters and machine coordinate system from the CL file;
  - 2) establish the solid model of the workpiece in the CAD/CAM system;
  - 3) construct the analytical tool swept volume using equation [1.33];
- 4) calculate the removal volume and updated in-process workpiece with equation [1.34] and equation [1.35];
- 5) set k = 1 and RV<sub>1</sub> = RV. RV<sub>k</sub> represents the solid model of the remaining removal volume after the trimming operation at the (k-1)th cutter location and to be cut at the kth cutter location;
- 6) generate the feasible contact surfaces  $\{Faces\}_{FCS,k}$  using equation [1.36] at the *k*th cutter location;
- 7) trim the solid model RV<sub>k</sub> by {Faces}<sub>FCS,k</sub>. Save the remaining part of RV<sub>k</sub> along the feed direction as RV<sub>k+1</sub>;
  - 8) search all boundary surfaces of  $RV_{k+1}$  and save them as  $\{Faces\}_{RV,k}$ ;

- 9) if the surface attributes of each  $\{Faces\}_{RV,k}$  are consistent with the surface attributes of the tool surface, append the surface into the sequence of the CWE surfaces  $\{Faces\}_{CWE,k}$  at the kth cutter location and repeat this step until all surfaces are considered:
- 10) calculate the intersection arcs in  $\{\text{Faces}\}_{\text{CWE},k}$  related to a set of discretized horizontal planes, which are perpendicular to the tool orientation and equivalently placed with equivalent length  $\Delta z$  along the tool orientation from the tool tip. Here,  $\Delta z$  is set to be  $z_{i,j}$ , i.e. the axial length of each edge disk of the cutter, as described in section 1.1.2;

Here, the intersection arcs include entry end point  $P_{k,en}$ , exit end point  $P_{k,ex}$  and center point  $C_k$  of arcs at the kth cutter location;

11) calculate the entry and exit angles at the kth cutter location using the following equations and the intersection arc data obtained from step (10):

$$\theta_{\text{en}} = \arcsin(\mathbf{f}_k \cdot \mathbf{r}_{k,\text{en}}), \ \theta_{\text{ex}} = \arcsin(\mathbf{f}_k \cdot \mathbf{r}_{k,\text{ex}})$$
 [1.41]

where  $\mathbf{f}_k$  is the feed direction vector at the kth cutter location, calculated using the CL data in step (1).  $\mathbf{r}_{k,\text{en}} = \mathbf{P}_{k,\text{en}} - \mathbf{C}_k$  and  $\mathbf{r}_{k,\text{ex}} = \mathbf{P}_{k,\text{ex}} - \mathbf{C}_k$ .  $\mathbf{P}_{k,\text{en}}$ ,  $\mathbf{P}_{k,\text{ex}}$  and  $\mathbf{C}_k$  are the coordinates of the entry end point, exit end point and center point obtained from step (10), respectively;

12) if  $k < N_{\rm CL} - 1$  , set k = k + 1 and go to step (6). Otherwise, stop the procedure.

#### 1.2.2.6. Numerical simulations

A ball end milling of an impeller is adopted to numerically check the validity of the method. An extraction algorithm is coded using C# and the application programming interface NX Open of SIEMENS NX 7.5. Instantaneous entry and exit angles are shown in Figure 1.12. During the engaging stage of the first-cut, the cutter-workpiece engagement area expands from the tip to the middle of the cutter until the continuous cutting stage starts. Corresponding to most parts of the cutter, engagement angles associated with following-cut are smaller than those related to first-cut, as shown in Figure 1.12. However, with respect to the ball end part, it follows the reverse conclusion due to the fact that the small radius at the ball end makes the cutting like a slot milling. Meanwhile, the efficiency of the proposed method is compared with the existing method described in [LAZ 11]. When 929 CL points in the above ball end milling are simulated,

the cost of the proposed method is about 424.2 seconds, while the cost of the method in [LAZ 11] is about 1716 seconds. This means the proposed method is more time-efficient.

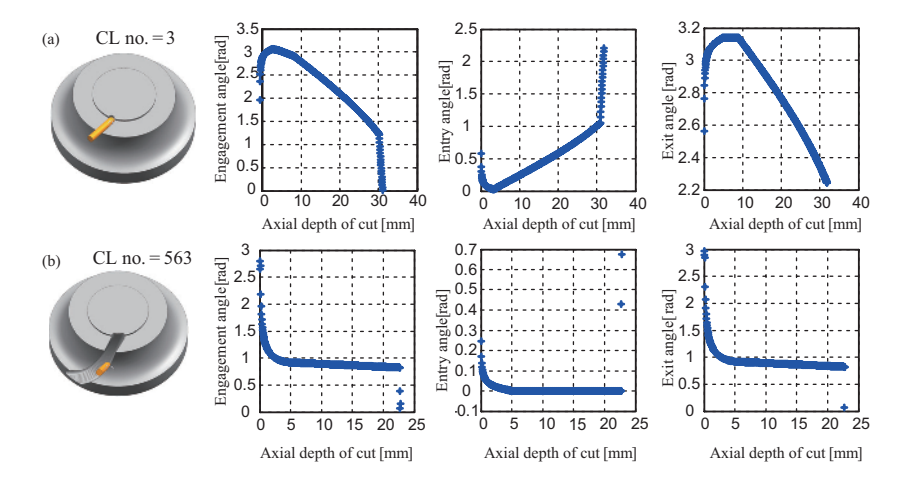


Figure 1.12. Ball end milling of an impeller at two different cutter locations

#### 1.3. Identification of the cutting force coefficients

In order to efficiently predict the cutting forces, it is of great importance to calibrate the values of cutting force coefficients and the cutter runout parameters *a priori*. In this book, four types of methods developed by the authors will be described in detail.

## 1.3.1. Calibration method for general end mills

This is a unified method suited to general end mills, such as flat end mill, bull nose end mill, ball end mill, etc. The cutter is firstly discretized into a finite number of disk elements. The total cutting forces are then obtained by summing the elemental forces acting on all sliced disk elements.

## 1.3.1.1. Identification of the cutting force coefficients

This scheme is generally developed based on the measured cutting forces. For a general end mill shown in Figure 1.2, at the cutting instant of angular position  $\theta_{i,j}(\varphi)$  for the jth axial disk element of the ith flute, the cyclic symmetry of the cutter flutes ensures that the jth axial disk element of the (i+k)th flute will have the same angular position, i.e.  $\theta_{i+k,j}(\varphi+2k\pi/N))=\theta_{i,j}(\varphi)$  after a cutter rotation of  $2k\pi/N$ . As a result, the sum of the cutting forces acting on the jth axial disk element of the ith (i=1,2,...,N) flute at the angular position  $\theta_{i,j}(\varphi)$  can be expressed as

$$\begin{bmatrix}
F_{X,j}(\varphi) \\
F_{Y,j}(\varphi) \\
F_{Z,j}(\varphi)
\end{bmatrix} = \mathbf{T}(\theta_{i,j}(\varphi)) \begin{bmatrix}
K_{T} \sum_{i=1}^{N} (h_{i,j}(\varphi)b_{i,j}) \\
K_{R} \sum_{i=1}^{N} (h_{i,j}(\varphi)b_{i,j}) \\
K_{A} \sum_{i=1}^{N} (h_{i,j}(\varphi)b_{i,j})
\end{bmatrix}$$
[1.42]

By reviewing equation [1.9] and equation [1.25] together with  $b_{i,j} = b_{k,j}$  (i, k = 1, 2, ..., N), we can obtain

$$\sum_{i=1}^{N} (h_{i,j}(\varphi)b_{i,j}) = z_{i,j} \{ Nf \sin \theta_{i,j}(\varphi) + \sum_{i=1}^{N} [r_{i,j} - r_{i-m,j}] \}$$
 [1.43]

with  $r_{i-m,j} = r_{N,j}$  if i - m = 0.

Because of  $\sum_{i=1}^{N} [r_{i,j} - r_{i-m,j}] = 0$ , the runout effect related to the last summation term of equation [1.43] can be naturally annulled so that

$$\sum_{i=1}^{N} (h_{i,j}(\varphi)b_{i,j}) = Nz_{i,j}f\sin\theta_{i,j}(\varphi)$$
[1.44]

Furthermore, by substituting equation [1.44] into equation [1.42] and then dividing equation [1.42] by N, we can obtain force components defined as

$$\begin{bmatrix}
\overline{F}_{\mathbf{X},j}(\varphi) \\
\overline{F}_{\mathbf{Y},j}(\varphi) \\
\overline{F}_{\mathbf{Z},j}(\varphi)
\end{bmatrix} = \frac{1}{N} \begin{bmatrix}
\sum_{i=1}^{N} F_{\mathbf{X},j}(\varphi) \\
\sum_{i=1}^{N} F_{\mathbf{Y},j}(\varphi) \\
\sum_{i=1}^{N} F_{\mathbf{Z},j}(\varphi)
\end{bmatrix} = z_{i,j} f \sin \theta_{i,j}(\varphi) \mathbf{T}(\theta_{i,j}(\varphi)) \begin{bmatrix} K_{\mathbf{T}} \\ K_{\mathbf{R}} \\ K_{\mathbf{A}} \end{bmatrix} [1.45]$$

From the above relation, it follows that  $\overline{F}_{s,j}(\varphi)$  (s=X,Y or Z) is independent of the cutter runout. In other words, equation [1.45] is just the nominal components of the cutting forces associated with the jth disk element of all flutes no matter what the cutter runout is.

Correspondingly, the total nominal cutting forces corresponding to  $\theta_{i,j}(\varphi)$  can be obtained by adding equation [1.45] along z

$$\begin{bmatrix}
\overline{F}_{\mathbf{X}}(\varphi) \\
\overline{F}_{\mathbf{Y}}(\varphi) \\
\overline{F}_{\mathbf{Z}}(\varphi)
\end{bmatrix} = \frac{1}{N} \begin{bmatrix}
\sum_{i=1}^{N} \left[ F_{\mathbf{X}}(\varphi + 2(i-1)\pi/N) \right] \\
\sum_{i=1}^{N} \left[ F_{\mathbf{Y}}(\varphi + 2(i-1)\pi/N) \right] \\
\sum_{i=1}^{N} \left[ F_{\mathbf{Z}}(\varphi + 2(i-1)\pi/N) \right]
\end{bmatrix} = f \mathbf{T}_{1}(\theta_{i,j}(\varphi)) \begin{bmatrix} K_{\mathbf{T}} \\ K_{\mathbf{R}} \\ K_{\mathbf{A}} \end{bmatrix} [1.46]$$

where

$$\mathbf{T}_{1}(\theta_{i,j}(\varphi)) = \begin{bmatrix} -\sum_{i,j} (z_{i,j}B_{2}) & -\sum_{i,j} (C_{1}B_{1}) & -\sum_{i,j} (C_{2}B_{1}) \\ \sum_{i,j} (z_{i,j}B_{1}) & -\sum_{i,j} (C_{1}B_{2}) & -\sum_{i,j} (C_{2}B_{2}) \\ 0 & \sum_{i,j} [C_{2}\sin\theta_{i,j}(\varphi)] - \sum_{i,j} [C_{1}\sin\theta_{i,j}(\varphi)] \end{bmatrix}$$
[1.47]

with

$$B_1 = \sin^2 \theta_{i,j}(\varphi), \quad B_2 = \sin \theta_{i,j}(\varphi) \cos \theta_{i,j}(\varphi)$$

$$C_1 = z_{i,j} \sin \kappa(z), \qquad C_2 = z_{i,j} \cos \kappa(z)$$
[1.48]

Here, the nominal cutting forces  $\overline{F}_s(\varphi)$  (s=X,Y or Z) are expressed as a linear function of the cutting force coefficients. Assume that  $F_s^{\rm M}(\varphi)$  (s=X,Y or Z) denotes measured values of cutting forces at cutter rotation angle  $\varphi$ . Following equation [1.46],  $\overline{F}_s(\varphi)$  can be approximated by averaging the measured values over one cutter revolution.

$$\overline{F}_s(\varphi) = \frac{1}{N} \sum_{i=1}^N [F_s^{M}(\varphi + 2(i-1)\pi/N)], \quad s = X, Y \text{ or } Z$$
 [1.49]

Finally, with the known values of  $\overline{F}_s(\varphi)$  (s=X, Y or Z),  $K_q$  (q=T, R or A) can be deduced immediately from equation [1.46] by the inverse of  $\mathbf{T}_1(\theta_{i,j}(\varphi))$ . Compared with existing methods, the main features of the proposed approach are twofold. On the one hand, a concise formulation independent of the cutter radial runout is established for the determination of cutting force coefficients. On the other hand, instantaneous values of the nominal cutting force components provide the possibility to investigate the instantaneous variation of the cutting force coefficients.

#### 1.3.1.2. Identification of the cutter runout parameters

Under the assumption of m=1, the substitution of equation [1.18] into equation [1.25] will give rise to the following equation

$$h_{i,j}^{c}(\varphi) = f \sin \theta_{i,j}(\varphi) + [-2\rho \sin(\frac{\pi}{N})) \sin(\lambda - \phi(z) - \frac{(2i-3)\pi}{N})]$$
 [1.50]

The condition m=1 implies that the current tooth removes the materials being left just by the previous one. Furthermore, by considering equations [1.50], [1.9], [1.8] and [1.14] together, equation [1.16] can be further developed as

$$\begin{bmatrix}
F_{\mathbf{X}}(\varphi) \\
F_{\mathbf{Y}}(\varphi) \\
F_{\mathbf{Z}}(\varphi)
\end{bmatrix} = f \mathbf{T}_{1}(\theta_{i,j}(\varphi)) \begin{bmatrix}
K_{\mathbf{T}} \\
K_{\mathbf{R}} \\
K_{\mathbf{A}}
\end{bmatrix} + \mathbf{T}_{2}(\theta_{i,j}(\varphi)) \begin{bmatrix}
\rho \cos \lambda \\
\rho \sin \lambda
\end{bmatrix}$$

$$= \begin{bmatrix}
\overline{F}_{\mathbf{X}}(\varphi) \\
\overline{F}_{\mathbf{Y}}(\varphi) \\
\overline{F}_{\mathbf{Z}}(\varphi)
\end{bmatrix} + \mathbf{T}_{2}(\theta_{i,j}(\varphi)) \begin{bmatrix}
\rho \cos \lambda \\
\rho \sin \lambda
\end{bmatrix}$$
[1.51]

with

$$\mathbf{T}_{2}(\theta_{i,j}(\varphi)) = \sin(\frac{\pi}{N}) \begin{bmatrix} A_{11}(\theta_{i,j}(\varphi)) & A_{12}(\theta_{i,j}(\varphi)) \\ A_{21}(\theta_{i,j}(\varphi)) & A_{22}(\theta_{i,j}(\varphi)) \\ A_{31}(\theta_{i,j}(\varphi)) & A_{32}(\theta_{i,j}(\varphi)) \end{bmatrix}$$
$$A_{11}(\theta_{i,j}(\varphi)) = \sum_{i,j} 2z_{i,j} \sin \gamma_{i,j} [K_{\mathrm{T}} \cos \theta_{i,j}(\varphi) + K_{\mathrm{R}} \sin \kappa(z) \sin \theta_{i,j}(\varphi)$$

 $+K_{\rm A}\cos\kappa(z)\sin\theta_{i,i}(\varphi)$ 

$$A_{12}(\theta_{i,j}(\varphi)) = \sum_{i,j} 2z_{i,j} \cos \gamma_{i,j} [K_{\mathsf{T}} \cos \theta_{i,j}(\varphi) + K_{\mathsf{R}} \sin \kappa(z) \sin \theta_{i,j}(\varphi) + K_{\mathsf{A}} \cos \kappa(z) \sin \theta_{i,j}(\varphi)]$$

$$A_{21}(\theta_{i,j}(\varphi)) = \sum_{i,j} 2z_{i,j} \sin \gamma_{i,j} [-K_{\mathsf{T}} \sin \theta_{i,j}(\varphi) + K_{\mathsf{R}} \sin \kappa(z) \cos \theta_{i,j}(\varphi) + K_{\mathsf{A}} \cos \kappa(z) \cos \theta_{i,j}(\varphi)]$$

$$A_{22}(\theta_{i,j}(\varphi)) = \sum_{i,j} 2z_{i,j} \cos \gamma_{i,j} [-K_{\mathsf{T}} \sin \theta_{i,j}(\varphi) + K_{\mathsf{R}} \sin \kappa(z) \cos \theta_{i,j}(\varphi) + K_{\mathsf{A}} \cos \kappa(z) \cos \theta_{i,j}(\varphi)]$$

$$A_{31}(\theta_{i,j}(\varphi)) = \sum_{i,j} 2z_{i,j} \sin \gamma_{i,j} [-K_{\mathbf{R}} \cos \kappa(z) + K_{\mathbf{A}} \sin \kappa(z)]$$

$$A_{32}(\theta_{i,j}(\varphi)) = \sum_{i,j} 2z_{i,j} \cos \gamma_{i,j} [-K_{\mathbf{R}} \cos \kappa(z) + K_{\mathbf{A}} \sin \kappa(z)]$$

$$\gamma_{i,j} = -\phi(z) - \frac{(2i-3)\pi}{N}$$

The first term of the right-hand side in equation [1.51] refers to a nominal component independent of cutter runout whereas the second term refers to the perturbation component due to cutter runout.

By combining equation [1.51] with equation [1.46], we can obtain

$$\mathbf{T_2}(\theta_{i,j}(\varphi)) \begin{bmatrix} \rho \cos \lambda \\ \rho \sin \lambda \end{bmatrix} = \begin{bmatrix} F_{\mathbf{X}}(\varphi) \\ F_{\mathbf{Y}}(\varphi) \\ F_{\mathbf{Z}}(\varphi) \end{bmatrix} - \begin{bmatrix} \overline{F}_{\mathbf{X}}(\varphi) \\ \overline{F}_{\mathbf{Y}}(\varphi) \\ \overline{F}_{\mathbf{Z}}(\varphi) \end{bmatrix}$$
[1.52]

Obviously, with the measured cutting forces assigned to  $F_X(\varphi)$ ,  $F_Y(\varphi)$  and  $F_Z(\varphi)$  and the known values of  $K_T$ ,  $K_R$  and  $K_A$  calibrated based on equation [1.46], cutter runout parameters  $\rho$  and  $\lambda$  can be evaluated

immediately by virtue of equation [1.52]. However, as the measured data often involve noise signals that may perturb  $F_{\rm X}(\varphi)$ ,  $F_{\rm Y}(\varphi)$  and  $F_{\rm Z}(\varphi)$ , the accuracy of  $\rho$  and  $\lambda$  may be strongly deteriorated if equation [1.52] is directly used. Moreover, since the cutter runout leads to a redistribution of the cutting forces over different tooth periods, it is necessary to choose the measured cutting forces in different tooth periods when solving  $\rho$  and  $\lambda$ . In this way, the influence of the noise signals may be weaken to the lower degree. To do this, the force component that has the largest peak value, e.g.  $F_{\rm Y}(\varphi)$ , is generally adopted.

Using equation [1.52] and  $F_Y$  at the cutter rotation angles  $\varphi_i = \varphi + 2(i-1)/N$  (i=1, 2, ..., N), we can obtain

$$\mathbf{T_3} \begin{bmatrix} g_1 \\ g_2 \end{bmatrix} = \mathbf{F_0} \tag{1.53}$$

with

$$\mathbf{T_3} = \begin{bmatrix} A_{21}(\theta_{i,j}(\varphi_1)) & A_{22}(\theta_{i,j}(\varphi_1)) \\ \vdots & & \vdots \\ A_{21}(\theta_{i,j}(\varphi_i)) & A_{22}(\theta_{i,j}(\varphi_i)) \\ \vdots & & \vdots \\ A_{21}(\theta_{i,j}(\varphi_N)) & A_{22}(\theta_{i,j}(\varphi_N)) \end{bmatrix}$$

$$g_1 = \rho \cos \lambda$$
$$g_2 = \rho \sin \lambda$$

$$\mathbf{F_0} = \begin{bmatrix} F_Y(\varphi_1) - \overline{F}_Y(\varphi) \\ \vdots \\ F_Y(\varphi_i) - \overline{F}_Y(\varphi) \\ \vdots \\ F_Y(\varphi_N) - \overline{F}_Y(\varphi) \end{bmatrix}$$

By means of the least square theory,  $g_1$  and  $g_2$  can be determined by

$$\begin{bmatrix} g_1 \\ g_2 \end{bmatrix} = \begin{bmatrix} \mathbf{T}_3^{\mathsf{T}} \mathbf{T}_3 \end{bmatrix}^{-1} \begin{bmatrix} \mathbf{T}_3^{\mathsf{T}} \mathbf{F}_0 \end{bmatrix}$$
 [1.54]

Therefore, it turns out that when m = 1, we have

$$\lambda = \arctan(g_2/g_1)$$

$$\rho = g_1/\cos \lambda \quad \text{or} \quad \rho = g_1/\sin \lambda$$
[1.55]

Note that the correct  $\lambda$  should give rise to a positive value of  $\rho$ . However, from the above procedure, we can see that a set of  $\rho$  and  $\lambda$  can be available for each value of cutter rotation angle. For this reason, the real set of runout parameter is selected to be such a one that minimizes the squared difference between the simulated and measured cutting forces at all sampling instants.

In the particular case of N=2,  $\mathbf{T_3^TT_3}$  will become singular in equation [1.54].  $\rho$  and  $\lambda$  can be optimally selected to be those that satisfy equation [1.53] and minimize the squared difference between the simulated and measured cutting forces at all sampled instants. For a single flute cutter with N=1, the cutting forces are not influenced by cutter runout.

#### 1.3.1.3. Selection of cutting parameters

As stated above, the identification procedure of  $\rho$  and  $\lambda$  is based on the assumption of single tooth engagement (STE). That is, only one flute is in cut at any cutter rotation angle. This condition can be easily satisfied with a reasonable selection of radial depth of cut,  $a_{\rm e}$ , and axial depth of cut,  $a_{\rm p}$ . Critical values of  $a_{\rm e}$  and  $a_{\rm p}$  can be defined by the following cutting conditions: whenever the current tooth disengages from the workpiece, the next tooth has to be engaged with the workpiece immediately. This means that with critical  $a_{\rm e}$  and  $a_{\rm p}$ , any increase of  $a_{\rm e}$  or  $a_{\rm p}$  will lead to multiple teeth engagement (MTE), i.e. an engagement of at least two teeth simultaneously at some cutter rotation angles. For a general end mill, the condition of STE can be mathematically written as

$$\phi(a_{\rm p}) - \phi(a_{\rm pe}) + \frac{\pi}{2} + \arcsin\left(\frac{a_{\rm e} - R_{\rm cut}}{R_{\rm cut}}\right) < \frac{2\pi}{N}$$
 [1.56]

where  $a_{\rm pe}$  and  $R_{\rm cut}$  are the pseudo axial depth of cut that is not engaged and the maximum radius of the cutting edge point that is engaged with the workpiece, respectively, as defined in Figure 1.2.

This is the critical condition characterizing the dependence between critical values of  $a_{\rm e}$  and  $a_{\rm p}$ . Critical conditions are now illustrated for a three-fluted flat end mill, three-fluted bull nose end mill and four-fluted ball end mill in Figures 1.13(a), (b) and (c). Equation [1.56] can be applied to design the experimental set-up for calibration of instantaneous cutting force coefficients. If the measured signals of the cutting forces are not bright enough to clearly identify the case of STE, we can appropriately reduce values of  $a_{\rm e}$  or  $a_{\rm p}$ .

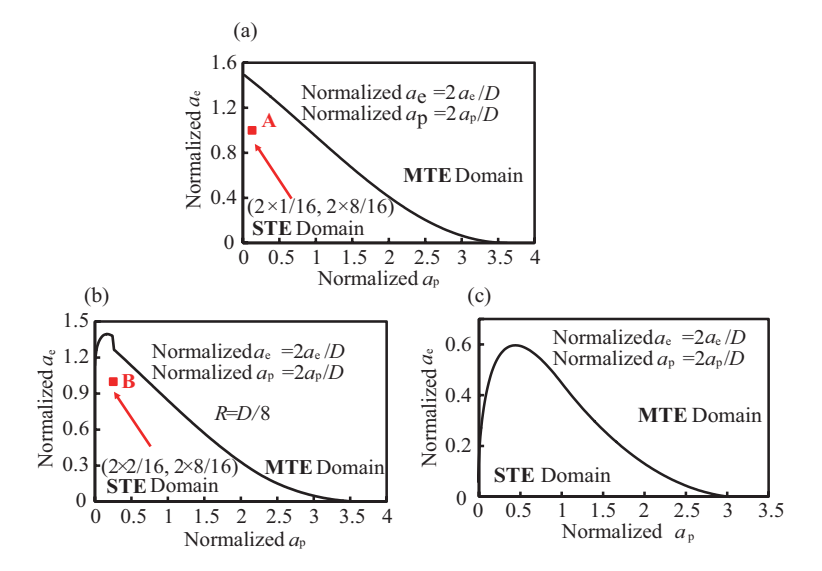


Figure 1.13. Critical curves describing the engagement of a single flute; a) Three-fluted flat end mill with a helix angle of 30°; b) Three-fluted bull nose end mill with a helix angle of 30°; c) Four-fluted ball end mill with a helix angle of 35°

However, one must keep in mind that equation [1.56] is derived with the negligence of the cutter runout. Practically, if one tooth is engaged in cut with an immersed axial length more than its nominal value due to runout, there must be at least another tooth that will be in cut with an immersed axial length less than its nominal value after some cutter rotation angles. As a result, STE will appear. Therefore, as long as  $a_e$  and  $a_p$  satisfy equation [1.56], the cutting test is in the state of STE regardless of the cutter runout.

#### 1.3.1.4. Test applications

To apply the above procedure, a series of cutting tests are performed in milling aluminum alloy 2618 with a vertical CNC milling machine. Three-component dynamometer Kistler 9255B is used to measure the cutting forces. A three-fluted carbide flat end mill with a diameter of 16mm and a helix angle of 30° is studied, respectively. A test with  $a_{\rm p}=1$  mm,  $a_{\rm e}=8$  mm and f=0.05 mm/tooth is used to calibrate the cutting force coefficients as well as the runout parameters. The identified cutting force coefficients are plotted versus the instantaneous average chip thickness (IACT)  $\bar{h}(\phi)$ , as shown in Figure 1.14.

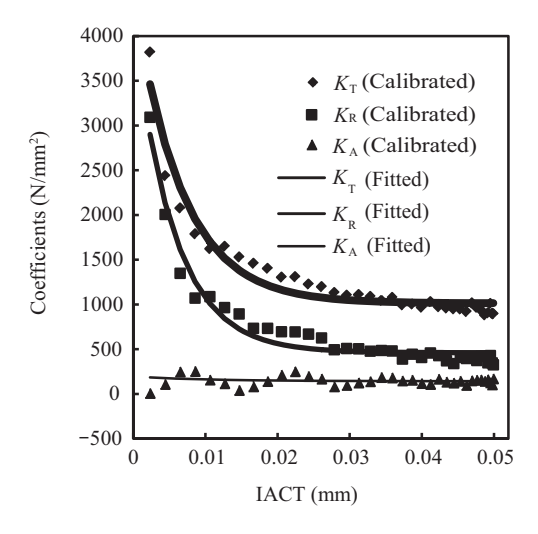


Figure 1.14. Calibrated cutting force coefficients

In Figure 1.14, we can see that an exponent-like relation exists between cutting force coefficients  $K_q$  ( $q=\mathrm{T},\mathrm{R}$  or A) and  $\overline{h}(\varphi)$ . For this reason, the relationship between  $K_q$  and  $\overline{h}(\varphi)$  is interpolated by the following nonlinear fitting function

$$K_q = W_{q1} + W_{q2}e^{[W_{q3}\bar{h}(\varphi)]}, \quad (q = T, R \text{ or } A)$$
 [1.57]

where  $W_{q1}$ ,  $W_{q2}$  and  $W_{q3}$  are constants determined by the fitting procedure. The fitted cutting force coefficients are also illustrated in Figure 1.14 for comparison with calibrated discrete values. With fitted values of  $K_q$ , runout parameters  $\rho$  and  $\lambda$  are then identified. Results are:  $\rho=5~\mu m$  and  $\lambda=60^\circ$ . Another test with  $a_p=1.3~mm$ ,  $a_e=8~mm$  and f=0.1~mm/tooth is used to verify the accuracy of calibrated cutting force model. From Figure 1.15, it can be seen that a good agreement exists between the predicted and measured cutting forces.

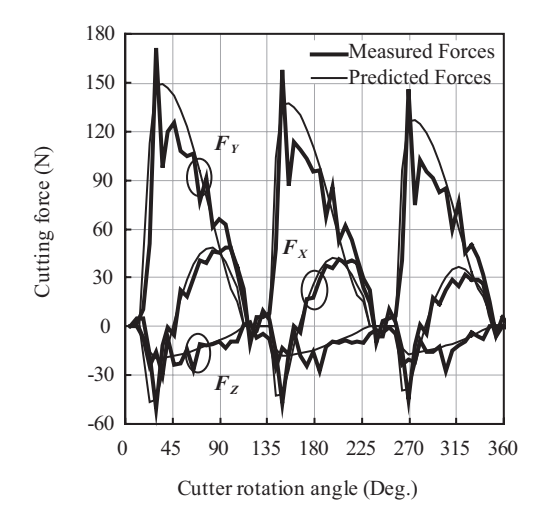


Figure 1.15. Comparison of measured and predicted cutting forces

## 1.3.2. Calibration method in the frequency domain

The cutting forces given in equation [1.8] are in the angle domain. Under the constant assumption of  $K_T$  and  $K_R$ , and m=1 in equation [1.25], the cutting forces can be expanded as follows in frequency domain through convolution analysis [LIA 94]

$$\begin{bmatrix} F_{\mathbf{X}}(\varphi) \\ F_{\mathbf{Y}}(\varphi) \end{bmatrix} = \sum_{k=-\infty}^{+\infty} \left\{ \begin{bmatrix} \mathbf{A}_{\mathbf{X}}[Nk] \\ \mathbf{A}_{\mathbf{Y}}[Nk] \end{bmatrix} e^{JNk\varphi} + \begin{bmatrix} \mathbf{A}_{\mathbf{XO}}[Nk+1] \\ \mathbf{A}_{\mathbf{YO}}[Nk+1] \end{bmatrix} e^{J(Nk+1)\varphi} + \begin{bmatrix} \mathbf{A}_{\mathbf{XO}}[Nk-1] \\ \mathbf{A}_{\mathbf{YO}}[Nk-1] \end{bmatrix} e^{J(Nk-1)\varphi} \right\}$$

$$= \begin{bmatrix} \mathbf{A}_{\mathbf{XO}}[Nk-1] \\ \mathbf{A}_{\mathbf{YO}}[Nk-1] \end{bmatrix} e^{J(Nk-1)\varphi}$$
[1.58]

with

$$\begin{bmatrix} \mathbf{A}_{\mathrm{X}}[Nk] \\ \mathbf{A}_{\mathrm{Y}}[Nk] \end{bmatrix} = \frac{N}{2\pi} \begin{bmatrix} -K_{\mathrm{T}} - K_{\mathrm{R}} \\ -K_{\mathrm{R}} & K_{\mathrm{T}} \end{bmatrix} \mathbf{P}_{\mathrm{e}}(Nk)CWD(Nk)$$

$$\begin{bmatrix} \mathbf{A}_{\mathrm{XO}}[Nk+1] \\ \mathbf{A}_{\mathrm{YO}}[Nk+1] \end{bmatrix} = \frac{N}{2\pi} J \rho \sin \frac{\pi}{N} e^{-J(\lambda + \frac{\pi}{N})} \begin{bmatrix} -K_{\mathrm{T}} - K_{\mathrm{R}} \\ -K_{\mathrm{R}} & K_{\mathrm{T}} \end{bmatrix} \mathbf{P}_{\mathrm{o}}(Nk+1)CWD(Nk)$$

$$\begin{bmatrix} \mathbf{A}_{\mathrm{XO}}[Nk-1] \\ \mathbf{A}_{\mathrm{YO}}[Nk-1] \end{bmatrix} = -\frac{N}{2\pi} J \rho \sin \frac{\pi}{N} e^{J(\lambda + \frac{\pi}{N})} \begin{bmatrix} -K_{\mathrm{T}} - K_{\mathrm{R}} \\ -K_{\mathrm{R}} & K_{\mathrm{T}} \end{bmatrix} \mathbf{P}_{\mathrm{o}}(Nk-1)CWD(Nk)$$

$$CWD(Nk) = \frac{D \sin \frac{Nka_{\mathrm{p}} \tan \beta}{D}}{Nk \tan \beta} e^{-JNk \frac{a_{\mathrm{p}} \tan \beta}{D}}$$

$$\mathbf{P}_{\mathrm{e}}(Nk) = \begin{bmatrix} P_{\mathrm{1}}[Nk] \\ P_{\mathrm{2}}[Nk] \end{bmatrix} = f \int_{\theta_{\mathrm{en}}}^{\theta_{\mathrm{ex}}} \begin{bmatrix} \sin \theta \cos \theta \\ \sin^{2} \theta \end{bmatrix} e^{-JNk\theta} d\theta$$

$$\mathbf{P}_{\mathrm{o}}(Nk) = \begin{bmatrix} P_{\mathrm{3}}[Nk] \\ P_{\mathrm{4}}[Nk] \end{bmatrix} = \int_{\theta_{\mathrm{en}}}^{\theta_{\mathrm{ex}}} \begin{bmatrix} \cos \theta \\ \sin \theta \end{bmatrix} e^{-JNk\theta} d\theta$$

where  $\mathbf{A}_s[Nk]$ ,  $\mathbf{A}_{sO}[Nk+1]$  and  $\mathbf{A}_{sO}[Nk-1]$  (s=X,Y) are the parameters related to the harmonics of the cutting forces predicted by equation [1.16]. J is unity of imaginary number.

In this section, the convolution theory-based method is described for the identification of the cutting force coefficients and radial cutter runout parameters, i.e.  $\rho$  and  $\lambda$  defined in Figure 1.5, for flat end mill. Details are explained and listed as follows.

 $F_{\rm X}(\varphi)$  and  $F_{\rm Y}(\varphi)$  can be expressed as

$$\begin{bmatrix} F_{\mathbf{X}}(\varphi) \\ F_{\mathbf{Y}}(\varphi) \end{bmatrix} = \begin{bmatrix} H_1(\varphi) & H_2(\varphi) \\ -H_2(\varphi) & H_1(\varphi) \end{bmatrix} \begin{bmatrix} K_{\mathbf{T}} \\ K_{\mathbf{R}} \end{bmatrix}$$
[1.59]

with

$$H_1(\varphi) = -\sum_{i,j} z_{i,j} h_{i,j}(\varphi) \cos \theta_{i,j}(\varphi)$$

$$H_2(\varphi) = -\sum_{i,j} z_{i,j} h_{i,j}(\varphi) \sin \theta_{i,j}(\varphi)$$
[1.60]

The Fourier series expansion of equation [1.59] can be written as

$$\begin{bmatrix} F_{\mathbf{X}}(\varphi) \\ F_{\mathbf{Y}}(\varphi) \end{bmatrix} = \left\{ \sum_{\omega = -\infty}^{+\infty} \begin{bmatrix} Q_{1}[\omega] & Q_{2}[\omega] \\ -Q_{2}[\omega] & Q_{1}[\omega] \end{bmatrix} e^{J\omega\varphi} \right\} \begin{bmatrix} K_{\mathbf{T}} \\ K_{\mathbf{R}} \end{bmatrix}$$
[1.61]

where  $Q_1[\omega]$  and  $Q_2[\omega]$  are the Fourier Transformations of  $H_1(\varphi)$  and  $H_2(\varphi)$ , respectively. Based on equation [1.58], the measured cutting forces  $F_s^M(\varphi)$  (s=X, Y) can be expanded as follows using Discrete Fourier Transformation.

$$\begin{bmatrix} F_{\mathbf{X}}^{\mathbf{M}}(\varphi) \\ F_{\mathbf{Y}}^{\mathbf{M}}(\varphi) \end{bmatrix} = \sum_{k=-\infty}^{+\infty} \left\{ \begin{bmatrix} \mathbf{A}_{\mathbf{X}}^{\mathbf{M}}[Nk] \\ \mathbf{A}_{\mathbf{Y}}^{\mathbf{M}}[Nk] \end{bmatrix} e^{JNk\varphi} + \begin{bmatrix} \mathbf{A}_{\mathbf{XO}}^{\mathbf{M}}[Nk+1] \\ \mathbf{A}_{\mathbf{YO}}^{\mathbf{M}}[Nk+1] \end{bmatrix} e^{J(Nk+1)\varphi} + \begin{bmatrix} \mathbf{A}_{\mathbf{XO}}^{\mathbf{M}}[Nk-1] \\ \mathbf{A}_{\mathbf{YO}}^{\mathbf{M}}[Nk-1] \end{bmatrix} e^{J(Nk-1)\varphi} \right\}$$
[1.62]

By combining equation [1.61] with equation [1.62] at  $\omega=Nk$ , the following relation can be obtained

$$\mathbf{B}[K_{\mathrm{T}}, K_{\mathrm{R}}]^{\mathrm{T}} = \mathbf{b} \tag{1.63}$$

with

$$\mathbf{b} = \left[ \operatorname{Re}(\mathbf{A}_{\mathbf{X}}^{\mathbf{M}}[Nk]), \operatorname{Im}(\mathbf{A}_{\mathbf{X}}^{\mathbf{M}}[Nk]), \operatorname{Re}(\mathbf{A}_{\mathbf{Y}}^{\mathbf{M}}[Nk]), \operatorname{Im}(\mathbf{A}_{\mathbf{Y}}^{\mathbf{M}}[Nk]) \right]^{\mathbf{T}}$$

$$\mathbf{B} = \begin{bmatrix} \operatorname{Re}(\mathbf{Q}_{1}[Nk]) & \operatorname{Re}(\mathbf{Q}_{2}[Nk]) \\ \operatorname{Im}(\mathbf{Q}_{1}[Nk]) & \operatorname{Im}(\mathbf{Q}_{2}[Nk]) \\ -\operatorname{Re}(\mathbf{Q}_{2}[Nk]) & \operatorname{Re}(\mathbf{Q}_{1}[Nk]) \\ -\operatorname{Im}(\mathbf{Q}_{2}[Nk]) & \operatorname{Im}(\mathbf{Q}_{1}[Nk]) \end{bmatrix}$$
[1.64]

where Re(\*) and Im(\*) indicate the real and imaginary parts of a complex number.

With the aid of equations [1.58] and [1.62],  $K_T$ ,  $K_R$ ,  $\rho$  and  $\lambda$  can be obtained using the method proposed by Liang and Wang [LIA 94].

$$\begin{bmatrix}
K_T \\
K_R
\end{bmatrix} = \begin{bmatrix}
-P_1(0) & -P_2(0) \\
P_2(0) & -P_1(0)
\end{bmatrix}^{-1} \begin{bmatrix}
\mathbf{A}_{\mathbf{X}}^{\mathsf{M}}[0] \\
\mathbf{A}_{\mathbf{Y}}^{\mathsf{M}}[0]
\end{bmatrix} \begin{bmatrix}
N \\
2\pi
\end{bmatrix} CWD(0)$$

$$\rho = \frac{|\mathbf{A}_{\mathbf{YO}}^{\mathsf{M}}[1]|}{\sin(\pi/N)(N/2\pi)a_{\mathsf{p}}|K_{\mathsf{T}}P_4(1) - K_{\mathsf{R}}P_3(1)|}$$

$$\lambda = \frac{\pi}{2} - \frac{\pi}{N} - \angle \mathbf{A}_{\mathbf{YO}}^{\mathsf{M}}[1] + \angle[K_{\mathsf{T}}P_4(1) - K_{\mathsf{R}}P_3(1)]$$
[1.65]

Details of this method and the definitions of  $P_1(0)$ ,  $P_2(0)$ , CWD(0),  $P_3(1)$  and  $P_4(1)$ , are given in [LIA 94].

The accuracy of equation [1.65] relies on the following two preconditions:

- the medial parameters involved in equation [1.62], e.g.  $\mathbf{A}_{\mathrm{X}}^{\mathrm{M}}[Nk]$ ,  $\mathbf{A}_{\mathrm{Y}}^{\mathrm{M}}[Nk]$ ,  $\mathbf{A}_{\mathrm{YO}}^{\mathrm{M}}[Nk+1]$ , etc., depend on the entry and exit angles, i.e.  $\theta_{\mathrm{en}}$  and  $\theta_{\mathrm{ex}}$ , which are calculated using equation [1.32] derived with nominal cutting parameters;
  - it is derived by assuming that m = 1.

However, the occurrence of cutter runout will greatly affect the actual cutting radius as well as  $\theta_{\rm en}$  and  $\theta_{\rm ex}$ . This means that the above two preconditions are not strictly satisfied when runout occurs. As a result, some accuracy will be lost if equation [1.65] is directly used. Note that, the larger the value of  $\rho$ , the greater the inaccuracy. To improve the calibration accuracy of equation [1.65], a new method is presented below.

With the aid of equation [1.63], an optimal selection procedure can be used to determine  $K_q$  (q=T,R),  $\rho$  and  $\lambda$  according to the following steps:

Step 1: Set  $\rho = \rho_0$  and  $\lambda = \lambda_0$ .  $\rho_0$  and  $\lambda_0$  are initially set by using equation [1.65].

Step 2: Calculate  $h_{i,j}(\varphi)$  by

$$h_{i,j}(\varphi) = \min_{m=1 \text{ to } N} \{ h_{i,j}(\varphi) = mf \sin \theta_{i,j}(\varphi) + r_{i,j} - r_{i-m,j} \}$$
 [1.66]

where  $r_{i,j}$  and  $r_{i-m,j}$  are obtained by equation [1.18].

- Step 3: Calculate  $Q_1[\omega]$  and  $Q_2[\omega]$  based on equations [1.60] and [1.66].
- Step 4: Calculate **B** using equation [1.64]. Then, by using the linear least square method,  $K_{\rm T}$  and  $K_{\rm R}$  can be immediately obtained by

$$\begin{bmatrix} K_{\rm T} \\ K_{\rm R} \end{bmatrix} = (\mathbf{B}^{\rm T} \mathbf{B})^{-1} \mathbf{B}^{\rm T} \mathbf{b}$$
 [1.67]

Step 5: Substitute  $K_{\rm T}$  and  $K_{\rm R}$  obtained from equation [1.67] into equation [1.59]. Then, calculate the minimum square deviation  $\delta(\rho,\lambda)$  between  $F_s^{\rm M}(\varphi)$  and  $F_s(\varphi)$  ( $s={\rm X,Y}$ ) by

$$\delta(\rho, \lambda) = \sum_{\varphi=0}^{2\pi} \left( \left| F_{\mathbf{X}}^{\mathbf{M}}(\varphi) - F_{\mathbf{X}}(\varphi) \right|^2 + \left| F_{\mathbf{Y}}^{\mathbf{M}}(\varphi) - F_{\mathbf{Y}}(\varphi) \right|^2 \right)$$
[1.68]

Step 6: If  $\delta(\rho, \lambda)$  achieves the level of minimum among all cases of different  $\rho$  and  $\lambda$ , set  $K_T$  and  $K_R$ ,  $\rho$  and  $\lambda$  as the final results of cutting force coefficients and runout parameters. Otherwise, repeat the above Steps 2 to 6 by setting  $\rho$  and  $\lambda$  to other values  $\rho_*$  and  $\lambda_*$ .

The key issue of the above steps is to optimally select  $\rho_*$  and  $\lambda_*$ . Generally, for every possible pairs of  $\rho_*$  and  $\lambda_*$  with  $\rho_{\min} \leq \rho_* \leq \rho_{\max}$  and  $\lambda_{\min} \leq \lambda_* \leq \lambda_{\max}$ , Step 2 to Step 6 will be performed. Here,  $\rho_{\max}$  and  $\rho_{\min}$  denote the maximum and minimum possible values of  $\rho_*$ ;  $\lambda_{\max}$  and  $\lambda_{\min}$  denote the maximum and minimum possible values of  $\lambda_*$ . The case which has the minimum  $\delta(\rho,\lambda)$  corresponds to the final result.

Obviously, this parametric study must sweep all cases in the feasible domain. To increase the computing efficiency, an automatical searching procedure will be described here.

The key is to approximately develop the explicit expressions that relate  $\rho$  and  $\lambda$  to  $F_s^{\mathbf{M}}(\varphi)$  and  $F_s(\varphi)$ . For this reason, it is interesting to study the following test case. The distributions of  $|\mathbf{A}_{\mathbf{Y}}[1]|$  and  $\angle \mathbf{A}_{\mathbf{Y}}[1]$  vs.  $\rho$  and  $\lambda$  are considered.  $\mathbf{A}_{\mathbf{Y}}[1]$  is obtained from  $F_{\mathbf{Y}}(\varphi)$  using the Fourier transformation.

 $F_{\rm Y}(\varphi)$  should be calculated from Step 5 for every selected set of  $\rho$  and  $\lambda$ .  $\rho$  and  $\lambda$  are chosen to vary from  $10^{-6}\mu{\rm m}$  to 35  $\mu{\rm m}$  and from 40° to 60°, respectively. The simulation results are shown in Figure 1.16. It can be found that both  $|{\bf A}_{\rm Y}[1]|$  and  $\angle{\bf A}_{\rm Y}[1]$  are approximately distributed in a planar surface over the considered region. This phenomenon indicates that  $|{\bf A}_{\rm Y}[1]|$  and  $\angle{\bf A}_{\rm Y}[1]$  can be locally treated as linear functions of  $\rho$  and  $\lambda$ . The same observations can also be made in other cutting conditions and regions of  $\rho$  and  $\lambda$ . Thus, following relations hold.

$$|\mathbf{A}_{Y}[1]| = E_{11}\rho + E_{12}\lambda + E_{13}$$

$$\angle \mathbf{A}_{Y}[1] = E_{21}\rho + E_{22}\lambda + E_{23}$$
[1.69]

where  $E_{uv}$  (u = 1, 2, v = 1, 2, 3) are unknown coefficients that can be determined using the finite difference scheme in the following way.

$$E_{11} = (|\mathbf{A}_{Y}[1]|_{3} - |\mathbf{A}_{Y}[1]|_{1})/\Delta \rho_{1}$$

$$E_{12} = (|\mathbf{A}_{Y}[1]|_{2} - |\mathbf{A}_{Y}[1]|_{1})/\Delta \lambda_{1}$$

$$E_{13} = |\mathbf{A}_{Y}[1]|_{1} - (E_{11}\rho_{1} + E_{12}\lambda_{1})$$

$$E_{21} = [(\angle \mathbf{A}_{Y}[1])_{3} - (\angle \mathbf{A}_{Y}[1])_{1}]/\Delta \rho_{1}$$

$$E_{22} = [(\angle \mathbf{A}_{Y}[1])_{2} - (\angle \mathbf{A}_{Y}[1])_{1}]/\Delta \lambda_{1}$$

$$E_{23} = (\angle \mathbf{A}_{Y}[1])_{1} - (E_{21}\rho_{1} + E_{22}\lambda_{1})$$
[1.70]

where  $\rho_1$ ,  $\lambda_1$  is a set of selected values satisfying  $\rho_{\min} \leq \rho_1$ ,  $\rho_2 \leq \rho_{\max}$  and  $\lambda_{\min} \leq \lambda_1$ ,  $\lambda_2 \leq \lambda_{\max}$ . Assume that  $\rho_2 = \rho_1 + \Delta \rho_1$ ,  $\lambda_2 = \lambda_1 + \Delta \lambda_1$ . With the aid of Steps 2 to 5, we can obtain  $|\mathbf{A}_Y[1]|_1$  and  $(\angle \mathbf{A}_Y[1])_1$  related to  $\rho_1$  and  $\lambda_1$ .  $|\mathbf{A}_Y[1]|_2$  and  $(\angle \mathbf{A}_Y[1])_2$  related to  $\rho_1$  and  $\lambda_2$ ,  $|\mathbf{A}_Y[1]|_3$  and  $(\angle \mathbf{A}_Y[1])_3$  related to  $\rho_2$  and  $\lambda_1$ .

Now,  $\rho_*$  and  $\lambda_*$  can be easily obtained by relating equation [1.69] to the experimental values of  $|A_Y^M[1]|$  and  $\angle A_Y^M[1]$  through

$$\begin{bmatrix} \rho_* \\ \lambda_* \end{bmatrix} = \begin{bmatrix} E_{11} & E_{12} \\ E_{21} & E_{22} \end{bmatrix}^{-1} \begin{bmatrix} A_{Y}^{M}[1] - E_{13} \\ \angle A_{Y}^{M}[1] - E_{23} \end{bmatrix}$$
[1.71]

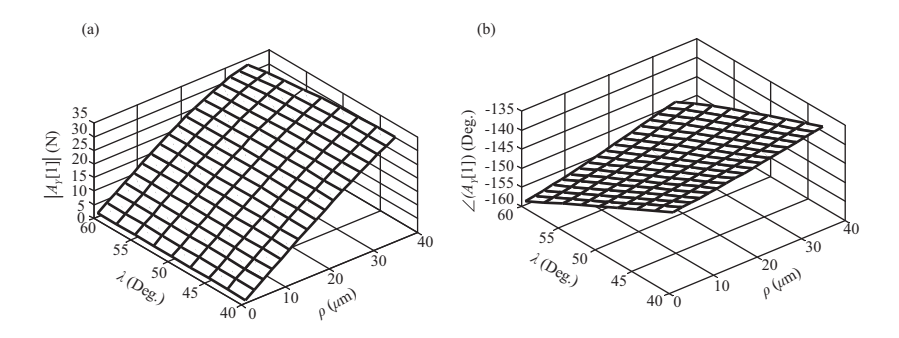


**Figure 1.16.** Distribution of  $|\mathbf{A}_{Y}[1]|$  and  $\angle \mathbf{A}_{Y}[1]$  v.s.  $\rho$  and  $\lambda$ ; a)  $|\mathbf{A}_{Y}[1]|$  v.s.  $\rho$  and  $\lambda$ ; b)  $\angle \mathbf{A}_{Y}[1]$  v.s.  $\rho$  and  $\lambda$ 

It is worth noting that as  $|\mathbf{A}_Y[1]|$  and  $\angle \mathbf{A}_Y[1]$  are linearly approximated over a local region, it is necessary to update the approximation on the new design point in an iterative way. This means that the coefficients  $E_{uv}$  involved in equation [1.70] need to be re-evaluated iteratively. As a result,  $K_q(q=\mathrm{T,R})$ ,  $\rho$  and  $\lambda$  should be iteratively determined according to the following steps:

Step a: Set  $\rho_1 = \rho_0$  and  $\lambda_1 = \lambda_0$ .

Step b: Calculate  $E_{uv}$  by means of equation [1.70].

Step c: Calculate  $\rho_*$  and  $\lambda_*$  using equation [1.71].

Step d: Set  $\rho = \rho_*$  and  $\lambda = \lambda_*$ . Then, repeat Steps 2 to 5.

Step e: If the error between two iterative results of  $\delta(\rho, \lambda)$  attains the prescribed tolerance, stop the iteration. Otherwise, repeat the above Steps b to e by attributing  $\rho_*$  and  $\lambda_*$  to  $\rho_1$  and  $\lambda_1$ .

## 1.3.3. Calibration method involving four cutter runout parameters

This method is mainly developed for the cutting force model, in which the cutting force coefficients are expressed as the exponential function of the instantaneous uncut chip thickness. That is, the elemental cutting forces related to the *j*th disk element of the *i*th flute are expressed as

$$F_{\mathrm{T},i,j}(\varphi) = K_{\mathrm{T}} h_{i,j}(\varphi) z_{i,j}$$

$$F_{\mathrm{R},i,j}(\varphi) = K_{\mathrm{R}} h_{i,j}(\varphi) z_{i,j}$$

$$F_{\mathrm{A},i,j}(\varphi) = K_{\mathrm{A}} h_{i,j}(\varphi) z_{i,j}$$
[1.72]

with

$$K_{\rm T} = k_{\rm T}[h_{i,j}(\varphi)]^{-m_{\rm T}}$$

$$K_{\rm R} = k_{\rm R}[h_{i,j}(\varphi)]^{-m_{\rm R}}$$

$$K_{\rm A} = k_{\rm A}[h_{i,j}(\varphi)]^{-m_{\rm A}}$$
[1.73]

where  $k_{\rm T}$ ,  $k_{\rm R}$ ,  $k_{\rm A}$ ,  $m_{\rm T}$ ,  $m_{\rm R}$  and  $m_{\rm A}$  are constants required to be determined from experiments.

Total cutting force components at cutter rotation angle  $\varphi$  can be obtained by

$$\begin{bmatrix}
F_{\mathbf{X}}(\varphi) \\
F_{\mathbf{Y}}(\varphi) \\
F_{\mathbf{Z}}(\varphi)
\end{bmatrix} = \sum_{i,j} \left\{ \mathbf{T}_{i,j}(\varphi) \begin{bmatrix} F_{\mathbf{T},i,j} \\
F_{\mathbf{R},i,j} \\
F_{\mathbf{Z},i,j} \end{bmatrix} \right\}$$
[1.74]

with

$$\mathbf{T}_{i,j}(\varphi) = \begin{bmatrix} -\cos\theta_{i,j}(\varphi) & -\sin\theta_{i,j}(\varphi) & 0\\ \sin\theta_{i,j}(\varphi) & -\cos\theta_{i,j}(\varphi) & 0\\ 0 & 0 & 1 \end{bmatrix}$$
[1.75]

It should be noted that  $h_{i,j}(\varphi)$  is calculated by equations [1.9] and [1.25], in which the calculation of the actual radius  $r_{i,j}$  of the circular tooth path includes the influence of cutter runout. In this section, two types of cutter runout models, i.e. radial and tilt cutter runout models, will be involved to reveal this effect:

- radial cutter runout model: its geometrical definition is given in section 1.2.1. In this model,  $r_{i,j}$  can be calculated by using equation [1.18];

- tilt cutter runout model: in this model, the actual installation state of the cutter is considered. That is, besides axis offset, there exists more or less axis tilt after the cutter is completely amounted in spindle, as shown in Figure 1.17. The geometry of this kind of cutter runout is characterized by four parameters, i.e.  $\rho_T$ ,  $\lambda_T$ ,  $\tau_T$  and  $\vartheta$ . Here,  $\rho_T$  and  $\tau_T$  are the axial offset and tilt angle between the cutter axis and the centerline of the spindle, respectively.  $\lambda_T$  is the location angle measured as the angle between the direction of the offset and the tip of the nearest tooth (tooth 1).  $\vartheta$  is the locating angle of tilt, which is defined as the angle between the direction of axis tilt and the direction of axial offset  $\rho_T$ . Note that L labeled in Figure 1.17 means the cantilevered length of cutter after installation. As shown in Figure 1.17, tilt cutter runout makes  $r_{i,j}$  change from  $\overline{AF}$  to  $\overline{OF}$ . Under this understanding,  $r_{i,j}$  can be calculated by

$$r_{i,j} = \{\rho_{\rm T}^2 + r_{{\rm n},i,j}^2 + (L - jz_{i,j})^2 \sin^2 \tau_{\rm T} + 2r_{{\rm n},i,j}\rho_{\rm T}\cos(-\lambda_{\rm T} + \phi(z) + \frac{2(i-1)\pi}{N}) + (1.76)\}$$

$$2((L - jz_{i,j})\sin \tau_{\rm T}[\rho_{\rm T}\cos(\phi) + r_{{\rm n},i,j}\cos(\vartheta - \lambda_{\rm T} + \phi(z) + \frac{2(i-1)\pi}{N})])\}^{\frac{1}{2}}$$

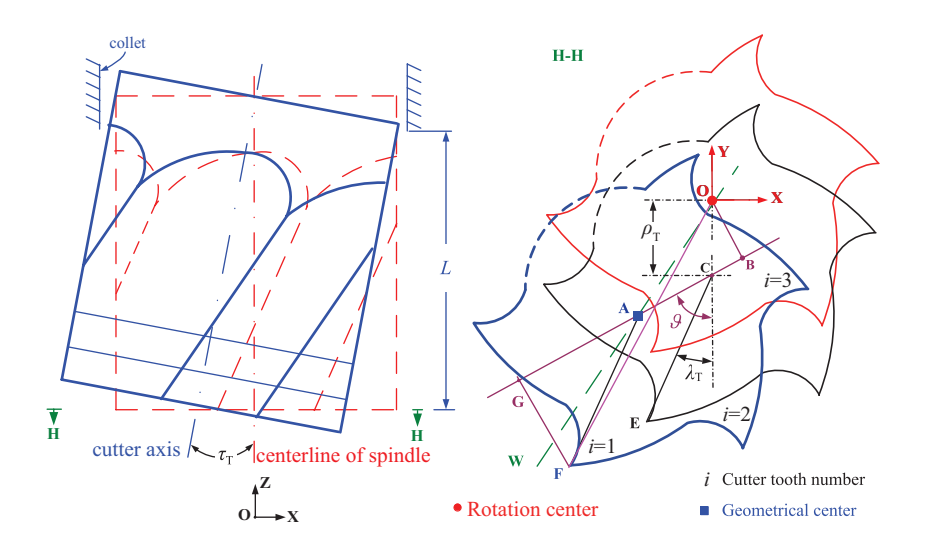


Figure 1.17. Definition of tilt cutter runout. For a color version of this figure, see www.iste.co.uk/zhang/milling.zip

By using the cutting forces measured from two milling tests, which satisfy the following two conditions, a new scheme will be proposed for calibrating the values of  $k_q$ ,  $m_q$  (q=T, R, A) and  $\rho_T$ ,  $\lambda_T$ ,  $\tau_T$  and  $\vartheta$ :

- radial and axial depths of cut of the first test, i.e.  $a_e$  and  $a_p$ , should satisfy equation [1.56] so that only one tooth is in contact with the workpiece at any cutter rotation angle  $\varphi$ . At the same time,  $a_p$  should be so small that  $z_{i,j}$  can be set to be  $a_p$ ;
- $-a_{\rm p}$  of the second test should be large enough, and generally it can be set to be the value greater than D. At the same time,  $a_{\rm e}$  should be relatively small so that the cutter cannot be broken under the combination of  $a_{\rm e}$  and  $a_{\rm p}$ .

Because  $a_{\rm p}$  in the first test is small, its cutter runout state in the range of  $0-a_{\rm p}$  along the cutter axis can be approximately treated as a radial cutter runout model. Consequently, the first test is adopted to calibrate  $k_q$ ,  $m_q$  ( $q={\rm T, R, A}$ ) and  $\rho$ ,  $\lambda$ . Then,  $\rho_{\rm T}$ ,  $\lambda_{\rm T}$ ,  $\tau_{\rm T}$  and  $\vartheta$  are calibrated based on the second test and the calibrated results from the first test. Detailed procedures are as follows.

### 1.3.3.1. Calibration of $k_q$ , $m_q$ (q = T, R, A) and $\rho$ , $\lambda$

Under the cutting condition of the first test, the cutting forces acting on the ith flute at an arbitrary cutter rotation angle  $\varphi$  constitute the total forces of the cutter. With this idea in mind, one can have

$$a_{\mathbf{p}} \begin{bmatrix} k_{\mathbf{T}}[h_{i,1}(\varphi)]^{1-m_{\mathbf{T}}} \\ k_{\mathbf{R}}[h_{i,1}(\varphi)]^{1-m_{\mathbf{R}}} \\ k_{\mathbf{A}}[h_{i,1}(\varphi)]^{1-m_{\mathbf{A}}} \end{bmatrix} = [\mathbf{T}_{i,1}(\varphi)]^{-1} \begin{bmatrix} F_{\mathbf{X}}^{\mathbf{M}}(\varphi) \\ F_{\mathbf{Y}}^{\mathbf{M}}(\varphi) \\ F_{\mathbf{A}}^{\mathbf{M}}(\varphi) \end{bmatrix}$$

$$\triangleq \begin{bmatrix} F_{\mathbf{T},i,1}^{\mathbf{M}}(\varphi) \\ F_{\mathbf{R},i,1}^{\mathbf{M}}(\varphi) \\ F_{\mathbf{A},i,1}^{\mathbf{M}}(\varphi) \end{bmatrix}$$
[1.77]

With the aids of equation [1.77],  $k_q$  and  $m_q$  (q = T, R, A),  $\rho_1$  and  $\lambda_1$  can be determined following the steps below:

Step 1: Set r=0 and set  $\rho^{(r)}=\rho_*$  and  $\lambda^{(r)}=\lambda_*$ .  $\rho_*$  and  $\lambda_*$  are the initially selected values. Practically,  $\rho_*$  and  $\lambda_*$  can be set to be the values close to zero. Here, r means the iteration step number.

Step 2: Calculate  $h_{i,1}^{(r)}(\varphi_k)$  for all cutter rotation angle  $\varphi_k$   $(k=1,\,2,\,\ldots,\,N_{\rm sp})$  related to all sampled cutting forces.  $N_{\rm sp}$  is the number of sampling points.

$$h_{i,1}^{(r)}(\varphi_k) = \min_{m=1}^{N} \left\{ mf \sin \theta_{i,1}(\varphi_k) + r_{i,1}^{(r)} - r_{i-m,1}^{(r)} \right\}$$
[1.78]

where  $r_{i,1}^{(r)}$  is calculated by equation [1.18].

Step 3: Establish the following relationship based on equations [1.77] and [1.78].

$$\mathbf{B}[k_{t}, m_{T}, k_{r}, m_{R}, k_{a}, m_{A}]^{T} = \mathbf{b}$$
 [1.79]

with 
$$k_{\rm t} = \ln(k_{\rm T}), k_{\rm r} = \ln(k_{\rm R}), k_{\rm a} = \ln(k_{\rm A})$$

$$\mathbf{B} = \begin{bmatrix} 1 & \ln[h_{i,1}^{(r)}(\varphi_{1})] & 0 & 0 & 0 & 0 \\ 1 & \ln[h_{i,1}^{(r)}(\varphi_{2})] & 0 & 0 & 0 & 0 \\ \vdots & \vdots & \vdots & \vdots & \vdots & \vdots & \vdots \\ 1 & \ln[h_{i,1}^{(r)}(\varphi_{N_{sp}})] & 0 & 0 & 0 & 0 & 0 \\ 0 & 0 & 1 & \ln[h_{i,1}^{(r)}(\varphi_{1})] & 0 & 0 & 0 \\ 0 & 0 & 1 & \ln[h_{i,1}^{(r)}(\varphi_{2})] & 0 & 0 & 0 \\ \vdots & \vdots & \vdots & \vdots & \vdots & \vdots & \vdots \\ 0 & 0 & 1 & \ln[h_{i,1}^{(r)}(\varphi_{N_{sp}})] & 0 & 0 & 0 \\ 0 & 0 & 0 & 0 & 1 & \ln[h_{i,1}^{(r)}(\varphi_{1})] & 0 & 0 \\ 0 & 0 & 0 & 0 & 1 & \ln[h_{i,1}^{(r)}(\varphi_{2})] & \vdots & \vdots & \vdots & \vdots \\ 0 & 0 & 0 & 0 & 1 & \ln[h_{i,1}^{(r)}(\varphi_{N_{sp}})] \end{bmatrix}$$

$$[1.80]$$

$$\mathbf{b} = \begin{bmatrix} \ln[F_{\mathrm{T},i,1}^{\mathrm{M}}(\varphi_{1})] - \ln[h_{i,1}^{(r)}(\varphi_{1})] - \ln(a_{\mathrm{p}}) \\ \ln[F_{\mathrm{T},i,1}^{\mathrm{M}}(\varphi_{2})] - \ln[h_{i,1}^{(r)}(\varphi_{2})] - \ln(a_{\mathrm{p}}) \\ \vdots \\ \ln[F_{\mathrm{T},i,1}^{\mathrm{M}}(\varphi_{N_{\mathrm{sp}}})] - \ln[h_{i,1}^{(r)}(\varphi_{N_{\mathrm{sp}}})] - \ln(a_{\mathrm{p}}) \\ \ln[F_{\mathrm{R},i,1}^{\mathrm{M}}(\varphi_{1})] - \ln[h_{i,1}^{(r)}(\varphi_{1})] - \ln(a_{\mathrm{p}}) \\ \ln[F_{\mathrm{R},i,1}^{\mathrm{M}}(\varphi_{2})] - \ln[h_{i,1}^{(r)}(\varphi_{2})] - \ln(a_{\mathrm{p}}) \\ \vdots \\ \ln[F_{\mathrm{R},i,1}^{\mathrm{M}}(\varphi_{N_{\mathrm{sp}}})] - \ln[h_{i,1}^{(r)}(\varphi_{N_{\mathrm{sp}}})] - \ln(a_{\mathrm{p}}) \\ \ln[F_{\mathrm{A},i,1}^{\mathrm{M}}(\varphi_{1})] - \ln[h_{i,1}^{(r)}(\varphi_{2})] - \ln(a_{\mathrm{p}}) \\ \vdots \\ \ln[F_{\mathrm{A},i,1}^{\mathrm{M}}(\varphi_{N_{\mathrm{sp}}})] - \ln[h_{i,1}^{(r)}(\varphi_{N_{\mathrm{sp}}})] - \ln(a_{\mathrm{p}}) \end{bmatrix}$$

where  $\ln{(*)}$  indicates the natural logarithm operation. Note that if  $h_{i,1}^{(r)}(\varphi_k)=0$  or  $F_{q,i,1}^{\rm M}(\varphi_k)<0$ , the corresponding row should be canceled from equation [1.79]

Step 4: Determine  $k_T$ ,  $m_T$ ,  $k_R$ ,  $m_R$ ,  $k_A$  and  $m_A$  by

$$[k_{t}, m_{T}, k_{r}, m_{R}, k_{a}, m_{A}]^{T} = (\mathbf{B}^{T} \mathbf{B})^{-1} \mathbf{B}^{T} \mathbf{b}$$

$$k_{T} = e^{k_{t}}, k_{R} = e^{k_{r}}, k_{A} = e^{k_{a}}$$
[1.82]

Step 5: Substitute  $k_q$  and  $m_q$  obtained from equation [1.82] into equation [1.74]. Then, calculate  $\Delta^{(r)}$  by

$$\Delta^{(r)} = \sum_{s=X,Y,Z} \sum_{k=1}^{N_{sp}} \left| F_s^{\mathsf{M}}(\varphi_k) - F_s(\varphi_k) \right|^2$$
 [1.83]

Step 6: If  $\Delta^{(r)}$  achieves the level of minimum among all cases of  $\rho^{(r)}$  and  $\lambda^{(r)}$ , set  $k_q$ ,  $m_q$ ,  $\rho^{(r)}$  and  $\lambda^{(r)}$  as the final results of cutting force coefficients

and radial cutter runout parameters  $\rho$  and  $\lambda$ . Otherwise, repeat the above Step 2 to Step 6 by setting  $\rho^{(r)}$  and  $\lambda^{(r)}$  to other values.

To increase the computing efficiency, an optimization algorithm, i.e. the Nelder-Mead simplex method [LAG 98, NEL 65], is adopted to select the best  $\rho^{(r)}$  and  $\lambda^{(r)}$  without the requirements of calculating the numerical or analytic gradients. The major idea about this algorithm is as follows. An initial simplex is firstly constructed. Then at each step of the search, a new point in or near the current simplex is generated. The function value at the new point is compared with the function's values at the vertices of the simplex and, usually, one of the vertices is replaced by the new point, giving a new simplex. This step is repeated until the diameter of the simplex is less than the specified tolerance. For details about this algorithm, one can refer to [LAG 98, NEL 65].

It is worth noting that in the above procedure  $a_p$  should be generally in the interval of [1 mm, 2 mm]. If  $a_p$  is too large, it can not be approximated by one disk element. If  $a_p$  is too small,  $F_s^{\rm M}(\varphi)$  (s=X,Y,Z) will be greatly influenced by the noise signals. As a result, equation [1.77] may lose validity.

#### 1.3.3.2. Calibration of $\rho_T$ , $\lambda_T$ , $\tau_T$ and $\vartheta$

If one treats the cutter installation state shown in Figure 1.17 as a radial cutter runout model, the following important relationship between tilt and radial cutter runout models can be obtained.

$$\rho = \overline{OA} = \sqrt{\overline{OB}^2 + \overline{BA}^2} = \sqrt{\overline{OB}^2 + (\overline{BC} + \overline{CA})^2}$$

$$\lambda = -\angle FAW$$

$$\angle FAG = \angle ECG$$
with
$$\overline{OB} = \rho_T \sin \vartheta$$

$$\overline{BC} = \rho_T \cos \vartheta$$

$$\overline{CA} = (L - jz_{i,j}) \sin \tau_T$$
[1.84]

Note that in this book the positive directions of  $\lambda_T$  and  $\lambda$  are defined as the clockwise direction. According to this definition,  $\lambda$  given in equation [1.84] is

negative. Further analysis of the geometry in Figure 1.17 gives the following relationship

$$\angle FAG = \angle FAW + \angle WAG = \angle FAW + \angle OAB$$

$$= \angle FAW + \sin\left(\frac{\overline{OB}}{\overline{OA}}\right)$$

$$\angle ECG = \vartheta - \lambda_T$$
[1.85]

By considering equations [1.84] and [1.85] together, one can obtain the following expressions

$$\rho^{2} = (\rho_{T} \sin \vartheta)^{2} + (\rho_{T} \cos \vartheta + (L - jz_{i,j}) \sin \tau_{T})^{2}$$

$$\arcsin \left(\frac{\rho_{T} \sin \vartheta}{\rho}\right) - \lambda = \vartheta - \lambda_{T}$$
[1.86]

Because  $z_{i,j} = a_p$  in the first cutting test, j = 1 can be achieved. With this idea in mind, equation [1.86] can be further simplified as.

$$\rho_{\rm T}^2 + 2\rho_{\rm T}(L - a_{\rm p})\sin\tau_{\rm T}\cos\vartheta + (L - a_{\rm p})^2\sin^2\tau_{\rm T} - \rho^2 = 0$$

$$\lambda_{\rm T} = \vartheta + \lambda - \sin\left(\frac{\rho_{\rm T}\sin\vartheta}{\rho}\right)$$
[1.87]

By solving the above quadratic equation, the following results are obtained

$$\rho_{\rm T} = \frac{-a + \sqrt{a^2 - 4c}}{2}$$

$$\lambda_{\rm T} = \vartheta + \lambda - \sin\left(\frac{\rho_{\rm T}\sin\vartheta}{\rho}\right)$$
[1.88]

with

$$a = 2(L - a_{p}) \sin \tau_{T} \cos \theta$$
$$c = (L - a_{p})^{2} \sin^{2} \tau_{T} - \rho^{2}$$

Based on equation [1.88],  $\rho_{\rm T}$ ,  $\lambda_{\rm T}$ ,  $\tau_{\rm T}$  and  $\vartheta$  are calibrated based on  $k_q$ ,  $m_q$  ( $q={\rm T,\,R,\,A}$ ) and  $\rho,\,\lambda$  calibrated from section 1.3.3.1 and  $F_s^{\rm M}(\varphi)$  measured from the second test.

Step 1: Set r=0 and set  $\vartheta^{(r)}=\vartheta_*,\, \tau^{(r)}_{\rm T}=\tau_{\rm T,*},\, \vartheta_*$  and  $\tau_{\rm T,*}$  are initial values usually close to zero.

Step 2: Calculate  $\rho_{\rm T}^{(r)}$  and  $\lambda_{\rm T}^{(r)}$  by using

$$\rho_{\text{T}}^{(r)} = \frac{-a + \sqrt{a^2 - 4c}}{2}, \ \lambda_{\text{T}}^{(r)} = \vartheta^{(r)} + \lambda - \arcsin(\frac{\rho_{\text{T}}^{(r)} \sin \vartheta^{(r)}}{\rho})$$

$$a = 2(L - a_{\text{p}}) \sin \tau_{\text{T}}^{(r)} \cos \vartheta^{(r)}, \ c = (L - a_{\text{p}})^2 \sin^2 \tau_{\text{T}}^{(r)} - \rho^2$$
[1.89]

Step 3: Calculate  $h_{i,j}^{(r)}(\varphi_k)$  for all cutter rotation angle  $\varphi_k$   $(k=1, 2, ..., N_{\rm SD})$ .

$$h_{i,j}^{(r)}(\varphi_k) = \min_{m=1}^{N} \left\{ mf \sin \theta_{i,j}(\varphi_k) + r_{i,j}^{(r)} - r_{i-m,j}^{(r)} \right\}$$
 [1.90]

where  $r_{i,j}^{(r)}$  is calculated by equation [1.76].

- Step 4: Substitute  $k_q$ ,  $m_q$  and  $h_{i,j}^{(r)}(\varphi_k)$  into equations [1.72] and [1.74] to predict  $F_s(\varphi_k)$ . Then, calculate  $\Delta^{(r)}$  with equation [1.83].
- Step 5: If  $\Delta^{(r)}$  achieves the level of minimum among all cases of  $\vartheta^{(r)}$  and  $\tau_{\rm T}^{(r)}$ , set  $\rho_{\rm T}^{(r)}$ ,  $\lambda_{\rm T}^{(r)}$ ,  $\tau_{\rm T}^{(r)}$  and  $\vartheta^{(r)}$  as the final results of  $\rho_{\rm T}$ ,  $\lambda_{\rm T}$ ,  $\tau_{\rm T}$  and  $\vartheta$ . Otherwise, set r=r+1 and the above Step 2 to Step 5 by setting  $\vartheta^{(r)}$  and  $\tau_{\rm T}^{(r)}$  to other values.

Similarly, to determine the values of  $\vartheta^{(r)}$  and  $\tau_{\rm T}^{(r)}$ , Nelder-Mead simplex method [LAG 98, NEL 65] is used. This idea together with Nelder-Mead simplex method can avoid the complex solving of nonlinear equations.

It is also worth noting that the proposed calibration procedures implies the following important understanding:

a) if tilt cutter runout model is considered, sections 1.3.3.1 and 1.3.3.2 should be combined to calibrate  $k_q$ ,  $m_q$  (q=T, R, A) and  $\rho_T$ ,  $\lambda_T$ ,  $\tau_T$ ,  $\vartheta$ . In this case, two cutting tests are needed;

b) whereas, if radial cutter runout model is considered, the calibration of  $k_q,\ m_q(q=T,R,A)$  and  $\rho,\lambda$  can be completed only by using section 1.3.3.1. In this case, only the first cutting test is needed.

#### 1.3.3.3. Model verification

Using the tests listed in the title of Table 1.2, the cutting force coefficients and runout parameters based on two cutter runout models are calculated and listed in Table 1.2. It is worth noting that with the procedures described in section 1.3.3.2, the calibrations of  $\rho_T$ ,  $\lambda_T$ ,  $\tau_T$  and  $\vartheta$  for tilt cutter runout model converge within 38 iteration steps. However, if we use one degree as the step length of  $\vartheta$  (0  $\leq \vartheta \leq 360^\circ$ ) and 0.001 degree as the step length of  $\tau$  (0  $\leq \tau \leq 0.06^\circ$ , 0.06° is an artificially given maximum bound) for parametric study, it requires about  $360 \times 60$  (= 21600) iteration steps. Furthermore, the calibrated results of  $\rho_T$ ,  $\lambda_T$ ,  $\tau_T$  and  $\vartheta$  from parametric study are:  $\rho_T = 14.53~\mu\text{m}$ ,  $\lambda_T = 132.79^\circ$ ,  $\tau_T = 0.028^\circ$  and  $\vartheta = 72^\circ$ . They are very close to those listed in Table 1.2.

	Radial cutter runout model	Tilt cutter runout model	
$k_{\rm T} \left({\rm N/mm}^2\right)$	758.17	758.17	
$m_{ m T}$	0.1723	0.1723	
$k_{\rm R} \left({\rm N/mm}^2\right)$	86.10	86.10	
$m_{\rm R}$	0.6609	0.6609	
$k_{\rm A} \left({\rm N/mm}^2\right)$	143.10	143.10	
$m_{\rm A}$	0.1555	0.1555	
Runout parameters	$\rho = 32.84 \ \mu \text{m}$ $\lambda = 85.69^{\circ}$	$ ho_{\rm T} = 14.50 \ \mu{\rm m}$	
	$\lambda = 85.69^{\circ}$	$\begin{aligned} \rho_{\mathrm{T}} &= 14.50 \; \mu \mathrm{m} \\ \lambda_{\mathrm{T}} &= 131.95^{\circ} \end{aligned}$	
		$\tau_{\rm T} = 0.02779^{\circ}$	
		$\theta = 70.85^{\circ}$	
Result source	Calibrated from Test 1	Calibrated from Tests 1 and 2	

**Table 1.2.** Calibrated results of cutting force coefficients and runout parameters based on different cutter runout models (for Test 1:  $a_{\rm e}=8$  mm,  $a_{\rm p}=2$  mm,  ${\rm f}=0.1667$  mm/tooth, spindle speed=1200 RPM; for Test 2:  $a_{\rm e}=0.8$  mm,  $a_{\rm p}=25$  mm, f=0.1 mm/tooth, spindle speed = 1000 RPM)

# 1.3.4. Identification of shear stress, shear angle and friction angle using milling tests

According to the oblique theory proposed by [ARM 85], the milling mechanism of the *i*th disk of the *i*th flute can be treated as an oblique cutting

process, as shown in Figure 1.18. From the viewpoint of the principle of force equilibrium,  $K_T$ ,  $K_R$  and  $K_A$  can be derived as [ALT 12]

$$K_{\rm T} = \frac{\tau_s}{\sin \psi_n} \frac{\cos(\beta_n - \alpha_n) + \tan \beta \tan \eta \sin \beta_n}{\sqrt{\cos^2(\psi_n + \beta_n - \alpha_n) + \tan^2 \eta \sin^2 \beta_n}}$$

$$K_{\rm R} = \frac{\tau_s}{\sin \psi_n \cos \beta} \frac{\sin(\beta_n - \alpha_n)}{\sqrt{\cos^2(\psi_n + \beta_n - \alpha_n) + \tan^2 \eta \sin^2 \beta_n}}$$

$$K_{\rm A} = \frac{\tau_s}{\sin \psi_n} \frac{\cos(\beta_n - \alpha_n) \tan \beta - \tan \eta \sin \beta_n}{\sqrt{\cos^2(\psi_n + \beta_n - \alpha_n) + \tan^2 \eta \sin^2 \beta_n}}$$
[1.91]

where  $\eta$  is chip flow angle. Equation [1.91] is a key bridge of orthogonal-to-oblique method that relates the cutting forces to the process geometric and physical parameters, i.e.  $\tau_{\rm s}$ ,  $\psi_{\rm n}$ ,  $\beta_{\rm n}$ ,  $\alpha_{\rm n}$  and  $\eta$ . More details on this derivation can be found in [ALT 12, BUD 96]. However the determination of shear stress  $\tau_{\rm s}$ , shear angle  $\psi_{n}$  and friction angle  $\beta_{n}$  involved in the cutting force model still resorted to abundant orthogonal cutting tests. For example, as reported in [ALT 12, BUD 96], more than 180 turning experiments were used for determination procedure. Instead of orthogonal turning, milling experiments are directly designed to determine shear stress, shear angle and friction angle in this section, and only a few milling tests are required for the determination procedure.

## 1.3.4.1. Determination of normal friction angle $\beta_n$

Figure 1.19(a) shows the geometric relations of cutting forces in normal plane  $P_{\rm n}$ . It can be found that

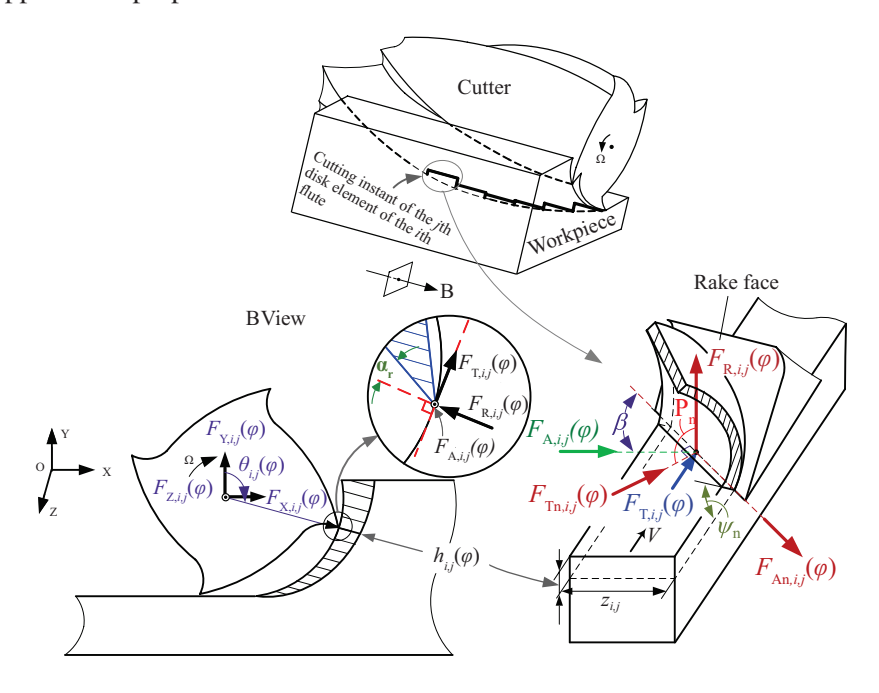
$$\tan(\beta_{\rm n} - \alpha_{\rm n}) = \tan\varphi_{\rm n} = \frac{F_{{\rm Rn},i,j}(\varphi)}{F_{{\rm Tn},i,j}(\varphi)} \text{ or } \beta_{\rm n} = \alpha_{\rm n} + \tan^{-1}\frac{F_{{\rm Rn},i,j}(\varphi)}{F_{{\rm Tn},i,j}(\varphi)}$$
[1.92]

with

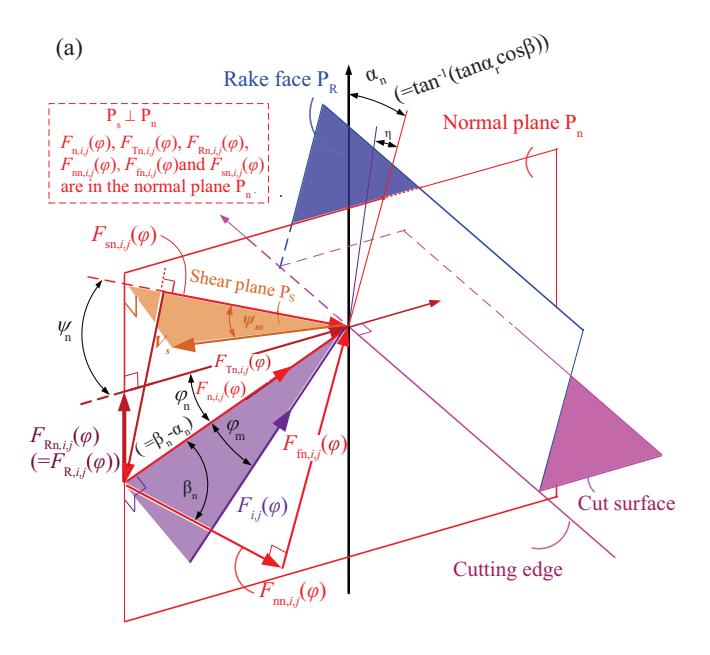
$$\alpha_{\rm n} = \tan^{-1}(\tan \alpha_{\rm r} \cos \beta) \tag{1.93}$$

where  $\alpha_r$  is radial rake angle of cutting edge.  $F_{\text{Rn},i,j}(\varphi)$  and  $F_{\text{Tn},i,j}(\varphi)$  are projections of  $F_{\text{R},i,j}(\varphi)$ ,  $F_{\text{T},i,j}(\varphi)$  and  $F_{\text{A},i,j}(\varphi)$  onto normal plane  $P_{\text{n}}$ , which is vertical to the cutting edge, as shown in Figures 1.18 and 1.19. Obviously,

if the values of  $F_{\mathrm{Rn},i,j}(\varphi)$  and  $F_{\mathrm{Tn},i,j}(\varphi)$  are available,  $\beta_{\mathrm{n}}$  can immediately be determined by using equation [1.92]. According to the theory in [ALT 12, BUD 96], cutting is uniform along the cutting edge in orthogonal turning process. Hence,  $F_{\mathrm{Rn},i,j}(\varphi)$  and  $F_{\mathrm{Tn},i,j}(\varphi)$  related to all disk elements are equal and collinear with the fixed thrust and feed directions. Thus, in turning process,  $\beta_{\mathrm{n}}$  can be determined by directly replacing  $F_{\mathrm{Rn},i,j}(\varphi)$  and  $F_{\mathrm{Tn},i,j}(\varphi)$  with the total cutting forces measured experimentally. However, in milling process, it is practically difficult to determine  $\beta_{\mathrm{n}}$  strictly from the measured cutting forces because of the following two factors. First, even at the same cutting instant, cutting forces associated with each disk element are different in magnitude and direction. Second, the measured cutting forces using dynamometer are available only in form of total cutting forces  $F_{\mathrm{s}}(\varphi)$  ( $s=\mathrm{X},\mathrm{Y},\mathrm{Z}$ ) and cannot be decomposed into force components related to each single disk element, i.e.  $F_{\mathrm{Rn},i,j}(\varphi)$  and  $F_{\mathrm{Tn},i,j}(\varphi)$ . Therefore, a new approach is proposed below.



**Figure 1.18.** Geometries and mechanics of flat end milling process. For a color version of this figure, see www.iste.co.uk/zhang/milling.zip



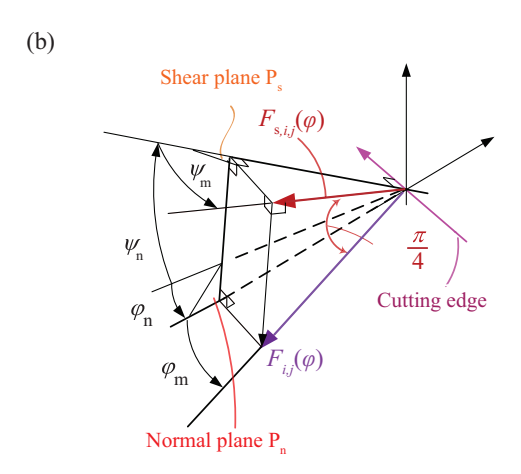


Figure 1.19. Cutting forces related to the jth axial disk element of the ith flute; a) General relationship in equivalent oblique cutting; b) Relative geometrical diagram. For a color version of this figure, see www.iste.co.uk/zhang/milling.zip

Total cutting forces can be deemed to be contributed by a single disk element under the following two conditions:

- 1) axial and radial depths of cut  $a_p$  and  $a_e$  satisfy equation [1.56]. That is, only one flute remains to be in cut at any engagement instant;
- 2)  $a_p$  is small enough so that it can be directly assigned to  $z_{i,j}$ . Generally,  $a_p$  can be selected within the range of 1–2 mm.

Based on a test under the above two conditions,  $F_{\mathrm{Rn},i,1}(\varphi)$ ,  $F_{\mathrm{Tn},i,1}(\varphi)$  and  $F_{\mathrm{An},i,1}(\varphi)$  shown in Figures 1.18 and 1.19 are then determined according to the following steps:

- 1) measure the total cutting forces  $\mathbf{F}_{\mathrm{XYZ}}^{\mathrm{M}}(\varphi)$  using a force dynamometer;
- 2) assume that  $[F_{X,i,1}(\varphi), F_{Y,i,1}(\varphi), F_{Z,i,1}(\varphi)]^T = \mathbf{F}_{XYZ}^{M}(\varphi);$
- 3) transform the measured forces  $\mathbf{F}_{\mathrm{XYZ}}^{\mathrm{M}}(\varphi)$  into tangential, radial and axial components by using the following equation:

$$[F_{\mathbf{T},i,1}(\varphi), F_{\mathbf{R},i,1}(\varphi), F_{\mathbf{A},i,1}(\varphi)]^{\mathrm{T}} = [\mathbf{T}(\theta_{i,1}(\varphi))]^{-1} \mathbf{F}_{\mathbf{XYZ}}^{\mathbf{M}}(\varphi)$$
[1.94]

4) calculate  $F_{\text{Rn},i,1}(\varphi)$ ,  $F_{\text{Tn},i,1}(\varphi)$  and  $F_{\text{An},i,1}(\varphi)$  based on the geometric relationship shown in Figure 1.18:

$$[F_{\text{Tn},i,1}(\varphi), F_{\text{Rn},i,1}(\varphi), F_{\text{An},i,1}(\varphi)]^{\text{T}} = \mathbf{T}(\beta)[F_{\text{T},i,1}(\varphi), F_{\text{R},i,1}(\varphi), F_{\text{A},i,1}(\varphi)]^{\text{T}}$$
[1.95]

Finally,  $\beta_n$  can be determined by substituting  $F_{Rn,i,j}(\varphi)$  and  $F_{Tn,i,j}(\varphi)$  obtained from equation [1.95] into equation [1.92].

## 1.3.4.2. Determination of shear angle $\psi_{\rm n}$ and chip flow angle $\eta$

The maximum shear stress principle indicates that shear occurs in the direction of maximum shear stress, where the angle between the shear velocity and the resultant force is  $\pi/4$ . The application of this principle to the milling process of the *j*th disk element of the *i*th flute leads to the reslutant force  $F_{i,j}(\varphi)$  making a  $\pi/4$  acute angle with the shear direction  $V_s$ , as shown in Figure 1.19(b). Mathematically, following relation holds for the shear force

 $F_{s,i,j}(\varphi)$ .

$$F_{s,i,j}(\varphi) = F_{i,j}(\varphi)(\cos\varphi_{m}\cos(\varphi_{n} + \psi_{n})\cos\psi_{m} + \sin\varphi_{m}\sin\psi_{m})$$

$$= F_{i,j}(\varphi)\cos\frac{\pi}{4}$$
[1.96]

Furthermore, because  $F_{s,i,j}(\varphi)$  is the maximum shear force on the shear plane, the component of the resultant force in the direction normal to the shear on the shear plane must be zero.

$$F_{i,j}(\varphi)(\cos\varphi_{\rm m}\cos(\varphi_{\rm n}+\psi_{\rm n})\sin\psi_{\rm m}-\sin\varphi_{\rm m}\cos\psi_{\rm m})=0 \qquad [1.97]$$

Solutions of equations [1.96] and [1.97] give

$$\sin \psi_{\rm m} = \sqrt{2} \sin \varphi_{\rm m} \tag{1.98}$$

$$\cos(\psi_{\rm n} + \varphi_{\rm n}) = \frac{\tan \varphi_{\rm m}}{\tan \psi_{\rm m}}$$
 [1.99]

Besides, according to [ALT 12], following geometric relations exist.

$$\sin \varphi_{\rm m} = \sin \beta_{\rm a} \sin \eta \tag{1.100}$$

$$\tan(\varphi_n + \alpha_n) = \tan \beta_a \cos \eta$$
 or  $\tan \beta_n = \tan \beta_a \cos \eta$  [1.101]

where  $\beta_a$  is the actual friction angle on the rake face. Chip flow angle  $\eta$  is generally assumed to equal helix angle  $\beta$  according to the chip flow rule proposed by [ALT 12].

Using  $\beta_n$  obtained in section 1.3.4.1 as the initial value, solutions of  $\psi_n$ ,  $\varphi_m$  and  $\varphi_n$  can be achieved by combining equations [1.98] to [1.101].

### 1.3.4.3. Determination of shear stress $\tau_{\rm s}$

Based on  $\psi_n$ ,  $\varphi_m$  and  $\varphi_n$  determined above, shear stress  $\tau_s$  can be calculated as

$$\tau_{s} = \frac{F_{s,i,1}(\varphi)}{A_{s,i,1}(\varphi)}$$

$$= \frac{F_{i,1}(\varphi)(\cos\varphi_{m}\cos(\varphi_{n} + \psi_{n})\cos\psi_{m} + \sin\varphi_{m}\sin\psi_{m})}{A_{s,i,1}(\varphi)} \quad [1.102]$$

where  $F_{i,1}(\varphi)$  is obtained by substituting the components of the measured forces  $\mathbf{F}_{M,XYZ}(\varphi)$  into the following equation.

$$F_{i,1}(\varphi) = \sqrt{(F_{X,i,1}^{M}(\varphi))^{2} + (F_{Y,i,1}^{M}(\varphi))^{2} + (F_{Z,i,1}^{M}(\varphi))^{2}}$$
[1.103]

 $A_{\mathrm{s},i,1}(\varphi)$  is calculated by

$$A_{s,i,1}(\varphi) = \frac{a_p}{\cos \beta} \frac{h_{i,1}(\varphi)}{\sin \psi_p}$$
 [1.104]

in which  $h_{i,1}(\varphi)$  can be calculated by using equations [1.9] and [1.25] if radial cutter runout parameters  $\rho$  and  $\lambda$  have been identified in advance. Alternatively, to ignore the effect of cutter runout, both  $F_{i,1}(\varphi)$  and  $h_{i,1}(\varphi)$  can be calculated using the nominal components.

As  $\varphi$  varies, the milling cutter undergoes a trochoidal motion that yields a continuous variation of chip thickness from zero to its maximum value, which in turn leads to the instantaneous cutting forces over a wide range of chip thickness. With these values, explicit expressions of  $\tau_s$ ,  $\beta_n$  and  $\psi_n$  can be established by treating  $\tau_s$ ,  $\beta_n$  and  $\psi_n$  as the functions of instantaneous uncut chip thickness.

The relations shown in Figure 1.20 are identified from two milling tests using carbide flat end mill and 7050 aluminum alloy. It can obviously be seen that  $\beta_n$  and  $\psi_n$  are the functions of uncut chip thickness. Figure 1.21 compares the measured cutting forces with the predicted ones by using the results from Figure 1.20.

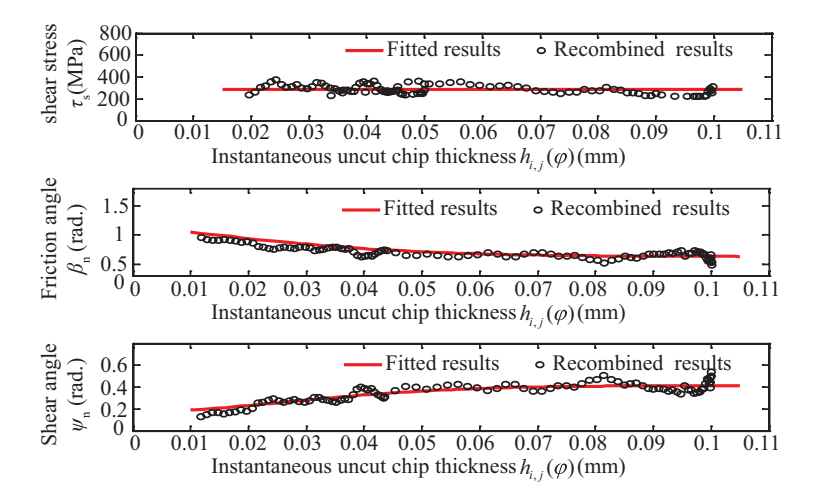
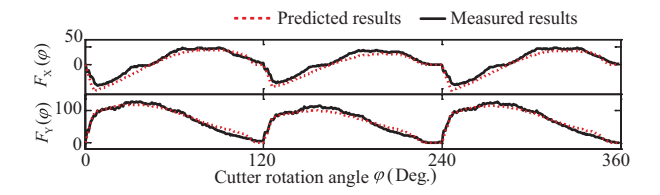


Figure 1.20. Results of stress, friction angle and shear angle. For a color version of this figure, see www.iste.co.uk/zhang/milling.zip



**Figure 1.21.** Comparisons of measured and predicted cutting forces. For a color version of this figure, see www.iste.co.uk/zhang/milling.zip

## 1.4. Ternary cutting force model including bottom edge cutting effect

A typical milling process of flat end mill is shown in Figure 1.22, from which it can be seen that both the flank edge and the bottom edge can be engaged with the workpiece during the actual cutting process. Thus, the calculation of the total cutting forces should include the contributions of the flank edge cutting and the bottom edge cutting effects. An illustration of

the force components is also shown in Figure 1.22. The total cutting forces can be expressed as

$$\mathbf{F}(\varphi) = \mathbf{F}_{\mathbf{F}}(\varphi) + \mathbf{F}_{\mathbf{B}}(\varphi) \tag{1.105}$$

where  $\mathbf{F}_F(\varphi)$  and  $\mathbf{F}_B(\varphi)$  are the cutting force vectors induced by flank and bottom edges at the cutter rotation angle  $\varphi$ . More details for the procedure of calculating  $\mathbf{F}_F(\varphi)$  and  $\mathbf{F}_B(\varphi)$  are given in the following.

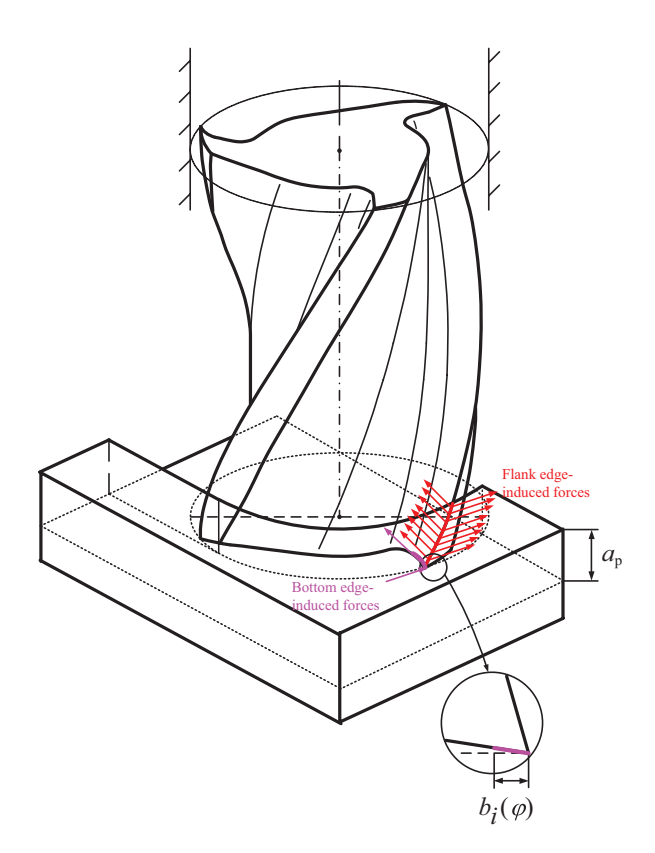


**Figure 1.22.** Flat end milling process. For a color version of this figure, see www.iste.co.uk/zhang/milling.zip

#### **1.4.1.** Calculations of $\mathbf{F}_{\mathbf{B}}(\varphi)$

The calculation of  $\mathbf{F}_{\mathrm{F}}(\varphi)$  can be carried out according to

$$\mathbf{F}_{F}(\varphi) = \begin{bmatrix} F_{X,F}(\varphi) \\ F_{Y,F}(\varphi) \end{bmatrix}$$
 [1.106]

$$F_{X,F}(\varphi) = \sum_{i,j} \left\{ g(\theta_{i,j}(\varphi)) [-F_{T,F,i,j}(\varphi) \cos \theta_{i,j}(\varphi) - F_{R,F,i,j}(\varphi) \sin \theta_{i,j}(\varphi)] \right\}$$

$$F_{Y,F}(\varphi) = \sum_{i,j} \left\{ g(\theta_{i,j}(\varphi)) [F_{T,F,i,j}(\varphi) \sin \theta_{i,j}(\varphi) - F_{R,F,i,j}(\varphi) \cos \theta_{i,j}(\varphi)] \right\}$$
[1.107]

with

$$\begin{split} F_{\text{T,F},i,j}(\varphi) &= K_{\text{Tc}} h_{\text{F},i,j}(\varphi) z_{i,j} + K_{\text{Te}} z_{i,j} \\ F_{\text{R,F},i,j}(\varphi) &= K_{\text{Rc}} h_{\text{F},i,j}(\varphi) z_{i,j} + K_{\text{Re}} z_{i,j} \\ h_{\text{F},i,j}(\varphi) &= \max\{0, \min_{m=1,2,\dots,N} \left[ mf \sin \theta_{i,j}(\varphi) + r_{i,j} - r_{i-m,j} \right] \} \end{split}$$

Note that in equation [1.108], the cutting mechanism of flank edge is characterized by dual mechanism model, in which the shearing effect and the rubbing effect of the flank edge are described separately.

## **1.4.2.** Calculations of $\mathbf{F}_{\mathcal{B}}(\varphi)$

The cutting mechanism of the bottom edge is likely the rubbing effect of the bottom edge rather than the shearing effect. Hence, the tangential force  $F_{\text{T.B.}i}(\varphi)$  and the radial force  $F_{\text{R.B.}i}(\varphi)$  related to the *i*th flute can be written as

$$F_{T,B,i}(\varphi) = K_{T,B}b_i(\varphi)$$

$$F_{R,B,i}(\varphi) = K_{R,B}b_i(\varphi)$$
[1.109]

where  $K_{T,B}$  and  $K_{R,B}$  are tangential and radial coefficients related to the bottom cutting effect of the bottom edge.  $b_i(\varphi)$  is the bottom uncut chip width

related to the *i*th bottom edge at the cutter rotation angle  $\varphi$ , as shown in Figure 1.22. Based on equation [1.109],  $\mathbf{F}_{B}(\varphi)$  can be calculated by

$$\mathbf{F}_{\mathrm{B}}(\varphi) = \begin{bmatrix} F_{\mathrm{X,B}}(\varphi) \\ F_{\mathrm{Y,B}}(\varphi) \end{bmatrix}$$
 [1.110]

with

$$F_{X,B}(\varphi) = g(\theta_{i,0}(\varphi))[-F_{T,B,i}(\varphi)\cos\theta_{i,0}(\varphi) - F_{R,B,i}(\varphi)\sin\theta_{i,0}(\varphi)]$$

$$F_{Y,B}(\varphi) = g(\theta_{i,0}(\varphi))[F_{T,B,i}(\varphi)\sin\theta_{i,0}(\varphi) - F_{R,B,i}(\varphi)\cos\theta_{i,0}(\varphi)]$$
[1.111]

where  $\theta_{i,0}(\varphi)$  is the angular position related to the *i*th flank edge tip at the cutter rotation angle  $\varphi$ .

Without the loss of generality, model calibration will be illustrated for equations [1.108] and [1.109]. Methods for the calibration of  $K_{qc}$ ,  $K_{qe}$  and  $K_{q,B}$  (q = T, R) are now described in detail.

## **1.4.3.** Calibration of $K_{qc}$ (q = T, R)

As long as the cutting is a single tooth engagement test with  $a_p$  being in the range of 1–2 mm, the total cutting forces measured in Cartesian X- and Y-directions can be transformed into tangential and radial components with good precision. Transformed tangential and radial forces show that they can linearly be approximated with respect to chip load  $\sum_{i,j} [h_{\mathrm{F},i,j}(\varphi)z_{i,j}]$ . This implies that the cutting force coefficients related to chip removal effect can be treated as constants. Based on this fact,  $K_{q\mathrm{c}}$  is calibrated by virtue of the transformed tangential and radial forces in following steps:

- 1) select experimental parameters under the condition that the axial depth of cut  $a_p$  is in the range of 1–2 mm;
- 2) identify radial cutter runout parameters  $\rho$  and  $\lambda$  experimentally or numerically;

- 3) measure the total cutting forces in X- and Y-directions by a force dynamometer;
  - 4) calculate  $h_{F,i,j}(\varphi)$  in terms of  $\rho$  and  $\lambda$  using equation [1.108];
  - 5) calculate chip load  $\sum_{i,j} [h_{F,i,j}(\varphi)z_{i,j}];$
- 6) transform the measured X- and Y-forces  $\mathbf{F}_{XY}^{M}(\varphi) = \left[\mathbf{F}_{X}^{M}(\varphi), \mathbf{F}_{Y}^{M}(\varphi)\right]^{T}$  into tangential and radial components by;

$$\mathbf{F}_{\mathrm{TR}}^{\mathrm{M}}(\varphi) = [\mathbf{T}(\theta_{i,0}(\varphi))]^{-1} \mathbf{F}_{\mathrm{XY}}^{\mathrm{M}}(\varphi)$$
 [1.112]

where  $\mathbf{F}_{TR}^{M}(\varphi) = \left[\mathbf{F}_{T}^{M}(\varphi), \mathbf{F}_{R}^{M}(\varphi)\right]^{T}$ .

- 7) plot  $F_q^{\rm M}(\varphi)$   $(q={\rm T,R})$  obtained from Step (6) as a function of chip load for each tooth;
- 8) use linear function to fit the relationship between  $F_q^{\rm M}(\varphi)$  and chip load for each tooth. The slope of each fitted line is symbolized as  $k_{i,q}$  ( $i=1,2,...,N,q={\rm T,R}$ );
  - 9) calculate  $K_{qc}$  by means of

$$K_{qc} = \sum_{i=1}^{N} k_{i,q}/N$$
 [1.113]

## **1.4.4.** Calibrations of $K_{q,B}$ (q = T, R)

Based on equation [1.106] and  $K_{qc}$  (q=T, R) calibrated above, the cutting force  $\mathbf{F}_{Fc}(\varphi)$ , which is related to shearing effect, can be calculated and then used together with the measured forces  $\mathbf{F}_{XY}^M(\varphi)$  to obtain the following components.

$$\mathbf{F}_{\mathrm{BFTR}}^{\mathrm{M}}(\varphi) = [\mathbf{T}(\theta_{i,0}(\varphi))]^{-1} [\mathbf{F}_{\mathrm{XY}}^{\mathrm{M}}(\varphi) - \mathbf{F}_{\mathrm{Fc}}(\varphi)]$$
 [1.114]

where  $\mathbf{F}_{BFTR}^{M}(\varphi) = \left[F_{BFT}^{M}(\varphi), F_{BFR}^{M}(\varphi)\right]^{T}$  stands for the experimental force component that only contains the flank rubbing and bottom edge cutting

effects. Combining this component with the prediction expression leads to the following equation.

$$\left[ \sum_{i,j} z_{i,j} \ b_i(\varphi) \right] \left[ \begin{matrix} K_{q\mathrm{e}} \\ K_{q,\mathrm{B}} \end{matrix} \right] = \mathrm{F}_{\mathrm{BF}q}^{\mathrm{M}}(\varphi), q = \mathrm{T}, \ \mathrm{R}$$
 [1.115]

At all sampling instants of the full engagement period, equation [1.115] can be expressed as

$$\mathbf{B}[K_{\text{Te}}, K_{\text{T,B}}, K_{\text{Re}}, K_{\text{R,B}}]^{\text{T}} = \mathbf{b}$$
 [1.116]

with

$$\mathbf{B} = \begin{bmatrix} \sum_{i,j} z_{i,j}(\varphi_1) & b_i(\varphi_1) & 0 & 0 \\ \vdots & \vdots & \vdots & \vdots \\ \sum_{i,j} z_{i,j}(\varphi_n) & b_i(\varphi_{N_{\text{sap}}}) & 0 & 0 \\ 0 & 0 & \sum_{i,j} z_{i,j}(\varphi_1) & b_i(\varphi_1) \\ \vdots & \vdots & \vdots & \vdots \\ 0 & 0 & \sum_{i,j} z_{i,j}(\varphi_n) & b_i(\varphi_{N_{\text{sap}}}) \end{bmatrix}$$
[1.117]

$$\mathbf{b} = \begin{bmatrix} F_{BFT}^{M}(\varphi_{1}) \\ \vdots \\ F_{BFT}^{M}(\varphi_{N_{\text{sap}}}) \\ F_{BFR}^{M}(\varphi_{1}) \\ \vdots \\ F_{BBP}^{M}(\varphi_{N_{\text{sap}}}) \end{bmatrix}$$
[1.118]

Based on equation [1.116],  $K_{qe}$  and  $K_{q,B}$  (q=T,R) can be determined by means of least-square fitting method.

$$[K_{\text{Te}}, K_{\text{T.B}}, K_{\text{Re}}, K_{\text{R.B}}]^{\text{T}} = [\mathbf{B}^{\text{T}}\mathbf{B}]^{-1}[\mathbf{B}^{\text{T}}\mathbf{b}]$$
 [1.119]

#### 1.4.5. Experimental work

Experiments are performed in a three-axis CNC vertical machining center for a three-fluted  $\phi$  16 Carbide end mill/aluminum AL 2618-T6 couple. The cutter is normal right-handed mill with helix angle of 30°. By using the above procedure, final results of the corresponding coefficients are as follows.

$$\begin{split} & [K_{\text{Tc}}, K_{\text{Rc}}, K_{\text{Te}}, K_{\text{Re}}, K_{\text{T,B}}, K_{\text{R,B}}]^{\text{T}} = \\ & [690.89\text{N/mm}^2, 179.32\text{N/mm}^2, 10.22\text{N/mm}, 10.20\text{N/mm}, 100.58\text{N/mm}, 66.54\text{N/mm}]^{\text{T}} \left[ 1.120 \right] \end{split}$$

Figure 1.23 shows the predicted cutting forces by using the model described in this section and the one given in section 1.3.1. It can be found that the proposed model holds the same order of prediction accuracy as the lumped force model described in section 1.3.1.

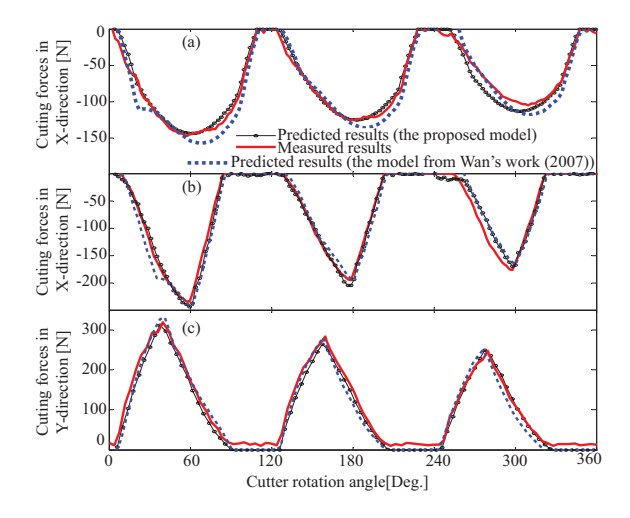


Figure 1.23. Comparisons of cutting forces predicted by two method. For a color version of this figure, see www.iste.co.uk/zhang/milling.zip

## 1.5. Cutting force prediction in peripheral milling of a curved surface

A typical peripheral milling of a curved surface is illustrated in Figure 1.24. XYZ is a globally stationary coordinate system attached to the

table, in which the workpiece boundary, the geometry of desired surface and the tool path are described.  $X_SY_SZ_S$  is a locally moving coordinate system attached to the spindle of the machine tool with its origin  $O_S$  at the center of the spindle.  $O_SX_S$  is aligned with the instantaneous feed direction of the theoretical tool path.  $O_SZ_S$  points upward along the spindle axis.  $O_SY_S$  is the normal to the feed direction and follows the definition of right-hand coordinate system. Then  $X_SY_SZ_S$  will move as the tool moves along the tool path.  $\theta_f(t)$  represents the angular location of the instantaneous feed direction  $O_SX_S$  and is measured anti-clockwise from the positive direction of X-axis at the sampling instant t.  $O_{TP}(t)$  and  $R_{TP}(t)$  denote the center of curvature and the radius of curvature related to tool position  $O_S(t)$  on the theoretical tool path, respectively.

Generally speaking, the tool position depends upon the parametric equation of theoretical tool path. The actual tool path generally used in NC machining is made up of a series of straight line segments and circular arc segments generated by the integrated CAM software, no matter how complex the theoretical tool path is. One such approximation can easily be used to determine the tool position without solving nonlinear equations and the computing time is largely saved. Mathematically, the actual tool position  $\mathbf{p}_a(t)$  is iteratively updated as

$$\mathbf{p}_{\mathrm{a}}(t+T_{\mathrm{s}}) = \begin{cases} \mathbf{p}_{\mathrm{a}}(t) + V_{\mathrm{f}}T_{\mathrm{s}}\mathbf{f}_{\mathrm{a}}(t) &, \text{ for linear tool path segment} \\ [\mathbf{R}] \left(\mathbf{p}_{\mathrm{a}}(t) - \mathbf{o}_{\mathrm{CTP}}\right) + \mathbf{o}_{\mathrm{CTP}}, \text{ for circular tool path segment} \end{cases}$$

with

$$\begin{split} \mathbf{f_a}(t) &= \frac{\mathbf{p_{en}} - \mathbf{p_{st}}}{|\mathbf{p_{en}} - \mathbf{p_{st}}|}, \\ [\mathbf{R}] &= \begin{bmatrix} \cos \alpha_{\rm s} - \sin \alpha_{\rm s} \ 0\\ \sin \alpha_{\rm s} & \cos \alpha_{\rm s} \ 0\\ 0 & 0 & 1 \end{bmatrix}, \\ \alpha_{\rm s} &= \frac{V_{\rm f} T_{\rm s}}{R_{\rm CTP}} \end{split}$$

where  $\mathbf{p}_{\mathrm{a}}(t) = [X_{\mathrm{a}}(t), Y_{\mathrm{a}}(t), 0]^{\mathrm{T}}$  is the tool position on the actual tool path.  $T_{\mathrm{s}}$  is a given sampling time interval.  $V_{\mathrm{f}}$  is the feed rate defined as the distance that the mill feeds as the spindle rotates one radian.  $\mathbf{f}_{\mathrm{a}}(t)$  is feed direction

of the cutter.  $o_{CTP}$  and  $R_{CTP}$  are center point and radius of a circular tool path segment.  $p_{st}$  and  $p_{en}$  are start point and end point of a linear tool path segment.

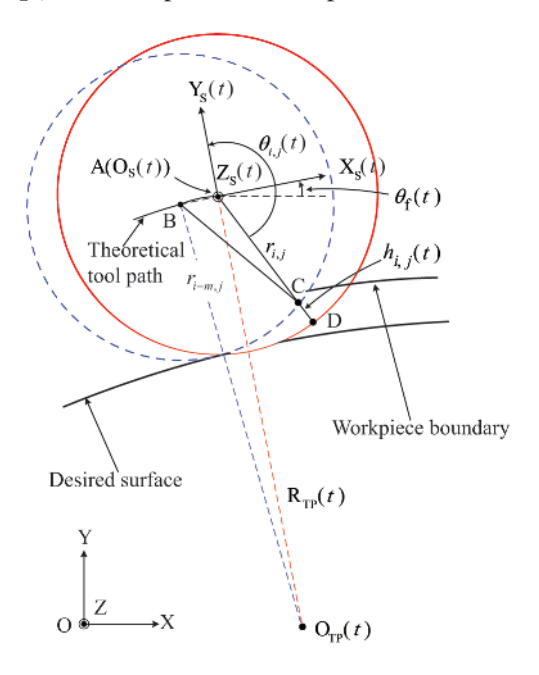


Figure 1.24. Representation of typical peripheral milling of a curved surface

Theoretically, the feed direction along the actual tool path might be easily determined by finding the tangential direction of the actual tool path. Nevertheless, if the tool position strides over the joint of two adjacent tool path segments, e.g. the joint of a straight line and a circle, as stated by Wei *et al.* [WEI 10], the feed direction, the exterior normal direction and the curvature of the actual tool path may be abruptly changed. In this section, the problem is avoided based on the concept of equivalent point obtained by mapping the tool position from the actual tool path to the theoretical one. The detailed procedures is presented below.

As shown in Figure 1.25,  $\mathbf{p}_{e}(t) = [X_{e}(u(t)), Y_{e}(u(t)), 0]^{T}$  is the equivalent tool position on the theoretical tool path defined by the intersection

(a)

point between the theoretical tool path and the normal of the actual tool path at  $\mathbf{p}_{a}(t)$ .

$$(\mathbf{p}_{e}(t) - \mathbf{p}_{a}(t)) \times \mathbf{n}_{a}(t) = \mathbf{0}$$
[1.122]

where  $\mathbf{n}_{a}\left(t\right)$  is the exterior normal of the actual tool path. u(t) is the parameter variable of the theoretical tool path.

$$\mathbf{n}_{\mathrm{a}}\left(t\right) = \begin{cases} \begin{bmatrix} 0 \ 0 \ 1 \end{bmatrix}^{\mathrm{T}} \times \mathbf{f}_{\mathrm{a}}(t), \text{ for linear tool path segment} \\ \mathbf{p}_{\mathrm{a}}(t) - \mathbf{o}_{\mathrm{CTP}} \ , & \text{for circular tool path segment (convex)} \\ \mathbf{o}_{\mathrm{CTP}} - \mathbf{p}_{\mathrm{a}}(t) \ , & \text{for circular tool path segment (concave)} \end{cases}$$

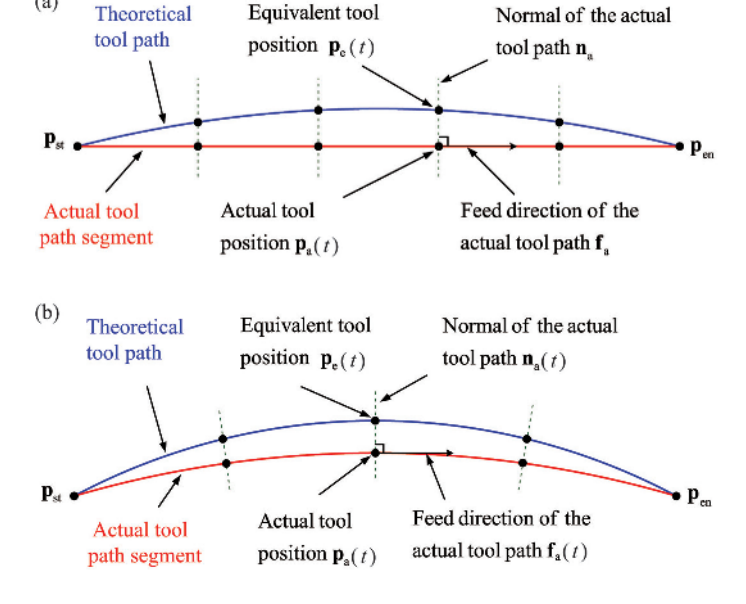


**Figure 1.25.** Interpolated tool position on the actual tool path: a) linear tool path segment and b) circular tool path segment

Geometrically, the equivalent feed direction of the cutter  $\mathbf{f}_{e}(t)$  can be defined as the tangential direction at  $\mathbf{p}_{e}(t)$ . It can be easily obtained by means of the value of u(t) solved from equation [1.122]. With  $\mathbf{f}_{e}(t)$  and u(t), the

exterior normal direction  $\mathbf{n_e}\left(t\right)$  and curvature  $K_{\mathrm{e}}\left(t\right)$  related to  $\mathbf{p_e}\left(t\right)$  are thus calculated by

$$\mathbf{n}_{e}(t) = \begin{bmatrix} 0 & 0 & 1 \end{bmatrix}^{T} \times \mathbf{f}_{e}(t)$$
 [1.124]

$$K_{e}(t) = \frac{X_{e}'(u(t))Y_{e}''(u(t)) - X_{e}''(u(t))Y_{e}'(u(t))}{\left(\left(X_{e}'(u(t))\right)^{2} + \left(Y_{e}'(u(t))\right)^{2}\right)^{\frac{3}{2}}}$$
[1.125]

In the following presentation,  $\mathbf{f}_{e}(t)$ ,  $\mathbf{n}_{e}(t)$  and  $K_{e}(t)$  are treated as the equivalent feed direction, equivalent exterior normal direction and equivalent curvature for the actual tool position  $\mathbf{p}_{a}(t)$ .

Besides, the angular location of the feed direction, i.e.  $\theta_f(t)$ , is calculated by the method reported in [WEI 10]

$$\theta_{\rm f}(t) = \arccos\left(\frac{\mathbf{f}_{\rm e}(t) \cdot \mathbf{I}_{\rm X}}{|\mathbf{f}_{\rm e}(t)|}\right)$$
 [1.126]

where  $\mathbf{I}_{X} = \begin{bmatrix} 1 \ 0 \ 0 \end{bmatrix}^{T}$  is the unit direction vector of X-axis.

Based on the geometries described above, the instantaneous uncut chip thickness and the entry and exit angles can be calculated as follows. Note that for the convenience of study, the cutter is discretized into disc elements with equal axial length  $z_{i,j}$ .

## 1.5.1. Calculations of instantaneous uncut chip thickness

In case of zero cutter runout, instantaneous uncut chip thickness can be expressed as an explicit function of feed per tooth and tooth positioning angle of the cutting point [KLI 82a, ALT 91, BUD 96, FEN 94a]. Conversely, instantaneous uncut chip thickness will be greatly redistributed in the presence of cutter runout and is generally calculated as the distance between two points, i.e. the cutting point related to the current circular path and the corresponding one at the previous circular path [KLI 83, SUT 86]. Explicit expressions relating the cutting parameters to cutter runout parameters were derived [KOE 61, SUT 86] only for straight surface milling. Here, an explicit

expression of instantaneous uncut chip thickness including the effect of cutter runout is derived for the milling of curved surface with variable curvature. For the milling of convex surfaces illustrated in Figure 1.24, suppose that the current cutting point D related to the *j*th disk element of the *i*th flute, is removing the surface left by the *m*th previous tooth. At the *m*th circular tooth path, the cutting point related to D is symbolized by C. The tool positions related to D and C are denoted by A and B, respectively. By definition, instantaneous uncut chip thickness related to the *j*th disc element of the *i*th flute can be expressed as

$$h_{i,j}(t,m) = L_{\text{CD}} = r_{i,j} - L_{\text{AC}}$$
 [1.127]

with  $r_{i,j}$  being calculated by equation [1.18].

Equation [1.127] indicates that the value of  $h_{i,j}(t,m)$  depends on  $L_{AC}$  whose calculation is as follows.

According to the triangle geometry relationship in  $\triangle ABC$ ,  $L_{AC}$  can be mathematically derived as:

$$L_{\text{AC}} = \sqrt{r_{i-m,j}^2 - \left(2R_{\text{TP}}(t)\sin\left(\frac{mf}{2R_{\text{TP}}(t)}\right)\cos\left(\frac{mf}{2R_{\text{TP}}(t)} + \theta_{i,j}(t)\right)\right)^2}$$
$$-2R_{\text{TP}}(t)\sin\left(\frac{mf}{2R_{\text{TP}}(t)}\right)\sin\left(\frac{mf}{2R_{\text{TP}}(t)} + \theta_{i,j}(t)\right)$$
[1.128]

where  $R_{\rm TP}\left(t\right)$  stands for the curvature related to arc. Theoretically, the radii of curvature and the centers of curvature related to tool positions A and B may be different due to the variable curvature of the theoretical tool path. Nevertheless, as the feed per tooth used is relatively small in practical milling and the curvature of arc between two adjacent tool positions A and B has a very mild variation, the curvature of the arc can be assumed to be a constant value equal to  $K_{\rm e}\left(t\right)$  and both A and B have the same curvature center  $O_{\rm TP}\left(t\right)$ . Mathematically, we have

$$R_{\text{TP}}(t) = \frac{1}{|K_{\text{e}}(t)|}$$
 [1.129]

Notice that the corresponding  $R_{TP}(t)$  should be recalculated by equations [1.125] and [1.129] once the tool position changes.

With the aid of equations [1.127] and [1.128], the instantaneous uncut chip thickness can be calculated by [DES 09]

$$h_{i,j}(t) = \max \left[0, \min_{m=1,2,\dots,N} (h_{i,j}(t,m))\right]$$
 [1.130]

Note that instantaneous uncut chip thickness can be obtained in a similar way in the case of milling of concave surfaces.

#### 1.5.2. Calculations of entry and exit angles

The presence of cutter runout not only influences instantaneous uncut chip thickness but also the entry/exit angles in the milling of curved surface. Desai et al. [DES 09] studied one such influence. In their computing of entry/exit angles, the intersection point between the tooth path and the theoretical workpiece boundary is obtained as long as the workpiece boundary is the parallel offset of the geometry of desired surface. However, when the workpiece boundary is not parallel to the geometry of desired surface, e.g. at the disengaging stage, results of entry or exit angles will be erroneous. Wei et al. [WEI 10] replaced the theoretical workpiece boundary with a set of straight line and circular arc segments, which are the parallel offset of tool path in pre-machining, i.e. the so-called actual workpiece boundary. Unfortunately, the influence of cutter runout was not considered in their work.

In this section, improvements are made on the calculation of exit angle at the engaging or disengaging stage including the influence of cutter runout. In the case of continuous engagement, entry and exit angles are obtained using the method in [DES 09]. At the engaging stage, as shown Figure 1.26, the exit angle can be obtained by

$$\theta_{\text{ex},i,j}\left(t\right) = \min_{m=1,2,\dots,N} \left(\theta_{\text{ex},i,j}\left(t,m\right), \theta_{\text{B,ex},i,j}\left(t\right)\right)$$
[1.131]

in which  $\theta_{\text{ex},i,j}$  (t,m) means the angle related to the intersection point of the current tooth path and the mth previous tool path corresponding to the *j*th disc element of the *i*th flute. It can be obtained by adopting the exit angle calculating method in [DES 09].  $\theta_{\text{B,ex},i,j}$  (t) is the angle related to the possible exit point,

which is the intersection of the current tooth path and the actual workpiece boundary.

$$\theta_{\mathrm{B,ex},i,j}\left(t\right) = \arccos\left(\frac{\left(\mathbf{p}_{\mathrm{w}}\left(v_{\mathrm{B,ex},i,j}\left(t\right)\right) - \mathbf{p}_{\mathrm{a}}\left(t\right)\right) \cdot \mathbf{n}_{\mathrm{e}}\left(t\right)}{\left|\mathbf{p}_{\mathrm{w}}\left(v_{\mathrm{B,ex},i,j}\left(t\right)\right) - \mathbf{p}_{\mathrm{a}}\left(t\right)\right| \left|\mathbf{n}_{\mathrm{e}}\left(t\right)\right|}\right)$$
[1.132]

where  $\mathbf{p}_{\mathrm{w}}(v_{\mathrm{B,ex},i,j}(t)) = [X_{\mathrm{w}}(v_{\mathrm{B,ex},i,j}(t)) \ Y_{\mathrm{w}}(v_{\mathrm{B,ex},i,j}(t)) \ 0]^{\mathrm{T}}$  means the parametric equations of actual workpiece boundary with  $v_{\mathrm{B,ex},i,j}(t)$  being the parameter variable of the workpiece boundary corresponding to the jth disc element of the ith flute. Although the rotation radius of the concerned disc element will deviate from its nominal value to  $r_{i,j}$  due to cutter runout [KLI 83, SUT 86, DES 09], the entry angle can still be obtained according to the method in [DES 09], as long as the rotation radius is replaced by  $r_{i,j}$ .

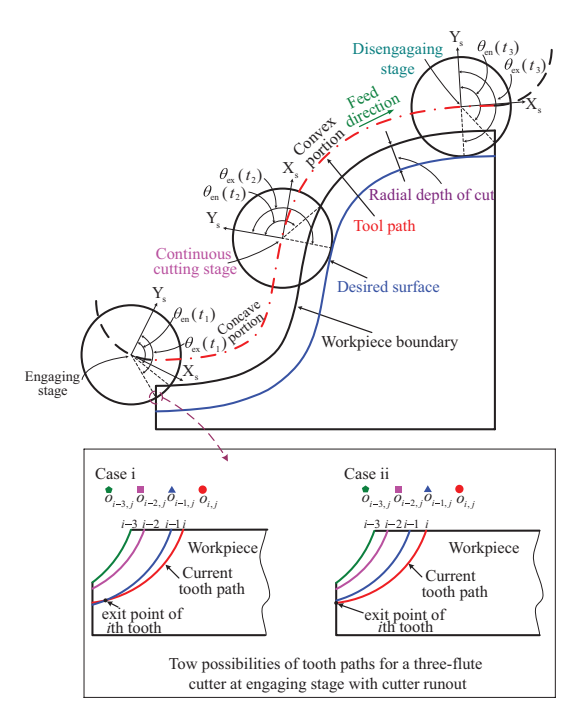


**Figure 1.26.** Entry/exit angles at different stages. For a color version of this figure, see www.iste.co.uk/zhang/milling.zip

Substitution of the instantaneous uncut chip thickness  $h_{i,j}(t)$  into equation [1.8] or equation [1.13] leads to the cutting force components  $F_{T,i,j}(t)$  and

 $F_{\mathrm{R},i,j}\left(t\right)$ , and then the total cutting force in locally moving coordinate system can be calculated as

$$F_{X_{S}}(t) = \sum_{i,j} g(\theta_{i,j}(t)) \left[ -F_{T,i,j}(t) \cos \theta_{i,j}(t) - F_{R,i,j}(t) \sin \theta_{i,j}(t) \right]$$

$$F_{Y_{S}}(t) = \sum_{i,j} g(\theta_{i,j}(t)) \left[ F_{T,i,j}(t) \sin \theta_{i,j}(t) - F_{R,i,j}(t) \cos \theta_{i,j}(t) \right]$$
[1.133]

where  $g(\theta_{i,j}(t))$  is obtained by substituting the entry angle  $\theta_{\text{en},i,j}(t)$  and exit angle  $\theta_{\text{ex},i,j}(t)$  into equation [1.15]. Due to the mobility of  $X_SY_SZ_S$ , the transformation into the globally stationary XYZ coordinate system corresponds to

$$F_{X}(t) = F_{X_{S}}(t) \cos \theta_{f}(t) - F_{Y_{S}}(t) \sin \theta_{f}(t)$$
  

$$F_{Y}(t) = F_{X_{S}}(t) \sin \theta_{f}(t) + F_{Y_{S}}(t) \cos \theta_{f}(t)$$
[1.134]

Based on the above procedure, the predicted cutting forces are plotted in Figure 1.27 along the entire tool path where the outline of the extreme value variations of the predicted cutting forces indicates that no abrupt change occurs along the entire tool path.

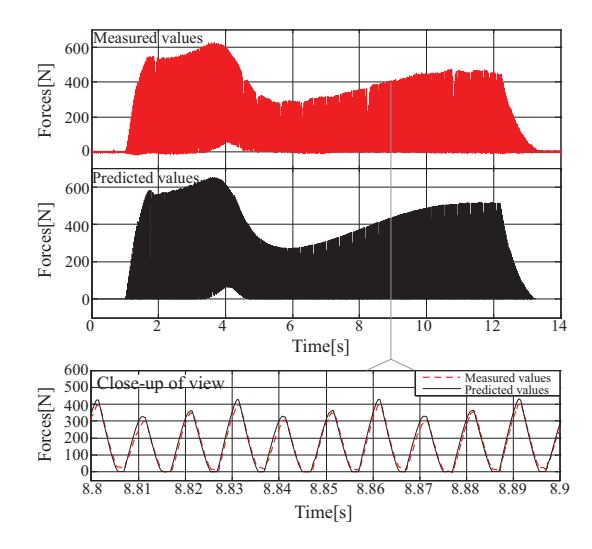


**Figure 1.27.** Comparison of the measured and predicted cutting forces in Y-direction vs. time for the entire tool path in test  $2(a_p=10 \text{ mm}, a_e=3 \text{ mm}, S=2000 \text{ RMP}, f=0.05 \text{ mm/tooth})$ . For a color version of this figure, see www.iste.co.uk/zhang/milling.zip